


Theoretical estimates of sulfoxyanion triple-oxygen equilibrium isotope effects and their implications

Journal Article

Author(s):

[Hemingway, Jordon](#) ; Goldberg, Madison L.; Sutherland, Kevin M.; Johnston, David T.

Publication date:

2022-11-01

Permanent link:

<https://doi.org/10.3929/ethz-b-000577336>

Rights / license:

[Creative Commons Attribution 4.0 International](#)

Originally published in:

Geochimica et Cosmochimica Acta 336, <https://doi.org/10.1016/j.gca.2022.07.011>

Funding acknowledgement:

946150 - Reconstructing the Effect of Sulfide Respiration on Global Redox State: Insights from Experiments, Observations, and Models (EC)



Contents lists available at ScienceDirect

Geochimica et Cosmochimica Acta

journal homepage: www.elsevier.com/locate/gca

Theoretical estimates of sulfoxyanion triple-oxygen equilibrium isotope effects and their implications



Jordon D. Hemingway^{a,b,*}, Madison L. Goldberg^b, Kevin M. Sutherland^b, David T. Johnston^b

^a Geological Institute, Department of Earth Sciences, ETH Zürich, Zürich, Switzerland

^b Department of Earth and Planetary Sciences, Harvard University, Cambridge, MA, USA

ARTICLE INFO

Article history:

Received 5 November 2021

Accepted 8 July 2022

Available online 22 July 2022

Associate editor: Marc Blanchard

Keywords:

Computational predictions

Microbial sulfate reduction

Pyrite oxidation

Sulfate

Triple-oxygen isotopes

ABSTRACT

Triple-oxygen isotope ($\delta^{18}\text{O}$ and $\Delta^{17}\text{O}$) analysis of sulfate is becoming a common tool to assess several biotic and abiotic sulfur-cycle processes, both today and in the geologic past. Multi-step sulfur redox reactions often involve intermediate sulfoxyanions such as sulfite, sulfoxylate, and thiosulfate, which may rapidly exchange oxygen atoms with surrounding water. Process-based reconstructions therefore require knowledge of equilibrium oxygen-isotope fractionation factors ($^{18}\alpha$ and $^{17}\alpha$) between water and each individual sulfoxyanion. Despite this importance, there currently exist only limited experimental $^{18}\alpha$ data and no $^{17}\alpha$ estimates due to the difficulty of isolating and analyzing short-lived intermediate species. To address this, we theoretically estimate $^{18}\alpha$ and $^{17}\alpha$ for a suite of sulfoxyanions—including several sulfate, sulfite, sulfoxylate, and thiosulfate species—using quantum computational chemistry. We determine fractionation factors for sulfoxyanion “water droplets” using the B3LYP/6-31G+(d,p) method; we additionally calculate higher-order method (CCSD/aug-cc-pVTZ and MP2/aug-cc-pVTZ) scaling factors, and we qualitatively estimate the importance of anharmonic zero-point energy (ZPE) corrections using a suite of gaseous sulfoxylate compounds. Methodological scaling factors greatly impact $^{18}\alpha$ predictions, whereas ZPE corrections are likely small (i.e., $\leq 1\%$) at Earth-surface temperatures; existing experimental data best agree with $^{18}\alpha$ predictions when including redox state-specific CCSD/aug-cc-pVTZ scaling factors. Theoretical pH- and temperature-specific bulk-solution (i.e., abundance-weighted average of all species) $^{18}\alpha$ values yield root-mean-square errors for sulfate/water, sulfite/water, and thiosulfate/water equilibrium of 4.5‰ ($n = 18$ experimental conditions), 3.7‰ ($n = 27$), and 2.2‰ ($n = 3$), respectively. However, sulfate- and sulfite-system agreement improves considerably when comparing experimental results only to $\text{SO}_3(\text{OH})^-/\text{H}_2\text{O}$ (RMSE = 1.6‰) and $\text{SO}_2(\text{OH})^-/\text{H}_2\text{O}$ (RMSE = 2.2‰) predictions, rather than bulk solutions. This is particularly true for the sulfite system at high and low pH, when $\text{SO}_2(\text{OH})^-$ is not the dominant species. We discuss potential experimental and theoretical biases that may lead to this apparent improvement. By combining $^{18}\alpha$ and $^{17}\alpha$ predictions, we additionally estimate that sulfate, sulfite, sulfoxylate, and thiosulfate species can exhibit $\Delta^{17}\text{O}$ values as much as 0.199‰, 0.205‰, 0.101‰, and 0.186‰ more negative than equilibrated water at Earth-surface temperatures (reference line slope = 0.5305). This theoretical framework provides a foundation to interpret experimental and observational triple-oxygen isotope results of several sulfur-cycle processes including pyrite oxidation, microbial metabolisms (e.g., sulfate reduction, thiosulfate disproportionation), and hydrothermal anhydrite precipitation. We highlight this with several examples.

© 2022 The Authors. Published by Elsevier Ltd. This is an open access article under the CC BY license (<http://creativecommons.org/licenses/by/4.0/>).

1. Introduction

Sulfur can exist in a range of redox states from S(-II) to S(+VI). As such, its oxidation and reduction represent major electron fluxes into and out of Earth's biosphere; these fluxes regulate

* Corresponding author at: Geological Institute, Department of Earth Sciences, ETH Zürich, Zürich, Switzerland.

E-mail address: jordon.hemingway@erdw.ethz.ch (J.D. Hemingway).

<https://doi.org/10.1016/j.gca.2022.07.011>

0016-7037/© 2022 The Authors. Published by Elsevier Ltd.

This is an open access article under the CC BY license (<http://creativecommons.org/licenses/by/4.0/>).

atmospheric O_2 content and the Earth-surface redox state over multi-million year timescales (Berner, 2001). Today, dissolved marine sulfate [S(+VI) redox state] constitutes one of the largest oxidant reservoirs on Earth's surface (Blättler et al., 2018), whereas sulfide minerals such as pyrite [FeS_2 ; S(-I)] contained in marine sediments and sedimentary rocks constitute one of the largest reductant reservoirs (Berner, 1984).

Several biotic and abiotic processes can transfer sulfur between these oxidized and reduced forms, often via sulfoxyanion species

that exist at intermediate redox states. For example, microbial sulfate reduction (MSR) is a metabolism that gains energy in the absence of O₂ by reducing dissolved sulfate to hydrogen sulfide [S(-II)]—the precursor to pyrite—via the intermediate species sulfite [S(+IV)] (Fike et al., 2015). Related metabolisms gain energy by simultaneously oxidizing and reducing sulfur to sulfate and sulfide via the disproportionation of intermediate redox compounds such as sulfite, zero-valent sulfur [S(0)], or the mixed-valence species thiosulfate [S(-I)/S(+V)]; see Vairavamurthy et al. (1993) for atom-specific redox state determination (Jørgensen, 1990; Fike et al., 2015). Similarly, the (a)biotic oxidative weathering of pyrite in exhumed rocks must occur via sulfite and thiosulfate intermediates, although the exact mechanism is complex and not fully constrained (e.g., Balci et al., 2007; Schoonen et al., 2010; Kohl and Bao, 2011). Furthermore, sulfoxyanion species existing in intermediate redox states are generally short-lived at Earth-surface conditions. For example, the hydrolysis and oxidation of sulfur dioxide gas [S(+IV)] to sulfate in atmospheric water—which represents a major pathway of acid rain formation—occurs on the order of microseconds (Brandt and van Eldik, 1995). The residence time of intracellular sulfite produced during MSR is similarly estimated to be on the order of microseconds before it is either fully reduced to hydrogen sulfide or reoxidized to sulfate (Bertran et al., 2020). Thus, even though the overall abundance of intermediate sulfoxyanions on Earth's surface at any point in time is low, nearly all sulfur-cycle processes require their transient production and consumption (e.g., Jørgensen, 1990).

One method to assess the relative importance of various sulfur-cycle processes is by analyzing the sulfur and oxygen isotope compositions of sulfate (³³S/³²S, ³⁴S/³²S, ³⁶S/³²S, ¹⁷O/¹⁶O, and ¹⁸O/¹⁶O; reported as Δ³³S, δ³⁴S, Δ³⁶S, Δ¹⁷O, and δ¹⁸O, respectively; see Section 2.1). For example, Wing and Halevy (2014) and Bertran et al. (2020) showed that ³⁴S and ¹⁸O fractionation during MSR represents an intermediate between kinetic and equilibrium fractionation factors; MSR rates in marine sediments can thus be predicted using the δ³⁴S and δ¹⁸O values of residual sulfate. Similarly, δ³⁴S, δ¹⁸O, and Δ¹⁷O values of dissolved sulfate in rivers has been used to estimate the relative importance of anaerobic pyrite weathering, aerobic pyrite weathering, and evaporite dissolution on land (e.g., Turchyn et al., 2013; Burke et al., 2018; Killingsworth et al., 2018; Hemingway et al., 2020; Burt et al., 2021; Kemeny et al., 2021). Furthermore, sulfate is preserved in minerals such as anhydrite/gypsum (CaSO₄), barite (BaSO₄), and carbonate (as carbonate-associated sulfate, or CAS); the sulfur and oxygen isotope compositions of these minerals can thus be used to reconstruct sulfur-cycle processes through time.

Despite the utility of sulfate isotopes as geologic tracers, their proper interpretation requires knowledge of fractionation factors for each step of each sulfur-cycle process. Although sulfur-isotope fractionation has been studied extensively (e.g., Eldridge et al., 2016; Eldridge et al., 2021), less is known about sulfoxyanion oxygen-isotope fractionation. Specific to δ¹⁸O and Δ¹⁷O, intermediate sulfoxyanions can rapidly exchange oxygen atoms with surrounding water, potentially exhibiting redox state- and species- or isomer-specific equilibrium fractionation factors (e.g., Pryor and Tonellato, 1967; Betts and Voss, 1970; Müller et al., 2013a; Wankel et al., 2014). Thus, the final oxygen isotope composition of sulfate produced or consumed by any process should depend strongly on (i) the isotope composition of water in which it formed and (ii) the specific intermediate sulfoxyanion species involved. Although some empirical ¹⁸O fractionation estimates exist for sulfate, sulfite, and thiosulfate (Lloyd, 1968; Chiba et al., 1981; Müller et al., 2013a; Wankel et al., 2014, this study), many sulfoxyanion oxygen-isotope fractionation factors—especially those for ¹⁷O—remain unknown due to the difficulty of experimentally measuring

these short-lived compounds. This lack of fractionation factor constraints hinders our ability to interpret sulfate δ¹⁸O and Δ¹⁷O values, both today and in the geologic past.

In the absence of experimental constraints, quantum-chemistry computational methods have been shown to yield acceptable triple-oxygen isotope fractionation factor estimates for a range of oxygen-containing anions and minerals (e.g., Cao and Liu, 2011; Hayles et al., 2018; Schauble and Young, 2021; Yeung and Hayles, 2021). Importantly, Δ¹⁷O estimates are particularly robust since any biases (e.g., arising from methodological inadequacies in potential energy surface calculations) largely cancel due to the mass-dependent nature of equilibrium ¹⁷O fractionation (Cao and Liu, 2011). Thus, if computational ¹⁸O fractionation factors can be shown to reasonably match experimental constraints, then Δ¹⁷O is expected to be accurate within analytical uncertainty.

Specific to sulfoxyanions, Eldridge et al. (2016) showed that different species of the same redox state (i.e., containing a different number of oxygen and/or hydrogen atoms due to hydration/dehydration) can exhibit unique sulfur-isotope fractionation factors; here, we hypothesize the same is true for oxygen isotopes. Additionally, protonated species likely control the rate at which oxygen atoms exchange with water. For example, Betts and Voss (1970) and Pryor and Tonellato (1967) showed that sulfite and thiosulfate exchange rates increase exponentially with decreasing pH due to the increasing abundance of species containing oxygen-bound protons, which are more reactive than non-protonated species. Because of this importance, we seek to computationally estimate triple-oxygen isotope fractionation factors for all major sulfoxyanion species. We specifically consider: (i) SO₄²⁻ and SO₃(OH)⁻ [S(+VI), collectively termed “sulfate”]; (ii) SO₃²⁻, (HS)O₃⁻, SO₂(OH)⁻, and dissolved SO_{2(aq)} gas [S(+IV), collectively termed “sulfite”]; (iii) SO₂²⁻, (HS)O₂⁻, SO(OH)⁻, (HS)O(OH), and S(OH)₂ [S(+II), collectively termed “sulfoxylate”]; and finally (iv) S₂O₃²⁻, (HS)SO₃⁻, and S₂O₂(OH)⁻ [mixed valence S(-I)/S(+V), collectively termed “thiosulfate”] (Fig. 1).

The remainder of this study is organized as follows: (i) first, we outline the necessary notation and quantum mechanical theory to computationally estimate triple-oxygen isotope fractionation factors (Section 2); (ii) next, describe the computational methods used, including those to estimate methodological scaling factors and the importance of anharmonic zero-point energy (ZPE) corrections (Section 3); (iii) we then report predicted fractionation factors and compare to available experimental results from the literature, including new experimental results included as part of this study (Section 4 and Supplementary Material); and finally (iv) we interpret these fractionation factors within the context of several sulfur-cycle processes and compare predictions to environmental data (Section 5). This work—combined with Eldridge et al. (2016) and Eldridge et al. (2021)—yields equilibrium fractionation factor estimates of all major and minor isotopes (³³S/³²S, ³⁴S/³²S, ³⁶S/³²S, ¹⁷O/¹⁶O, and ¹⁸O/¹⁶O) for several important sulfoxyanion species.

2. Theory

2.1. Notation

The oxygen-isotope composition of a given compound “A” can be written as

$$\delta^*O_A = \frac{^*R_A}{^*R_{VSMOW}} - 1, \quad (1)$$

where *R denotes the ^{*}O/¹⁶O ratio, “*” indicates the heavy isotope ¹⁷O or ¹⁸O, and VSMOW is the Vienna Standard Mean Ocean Water

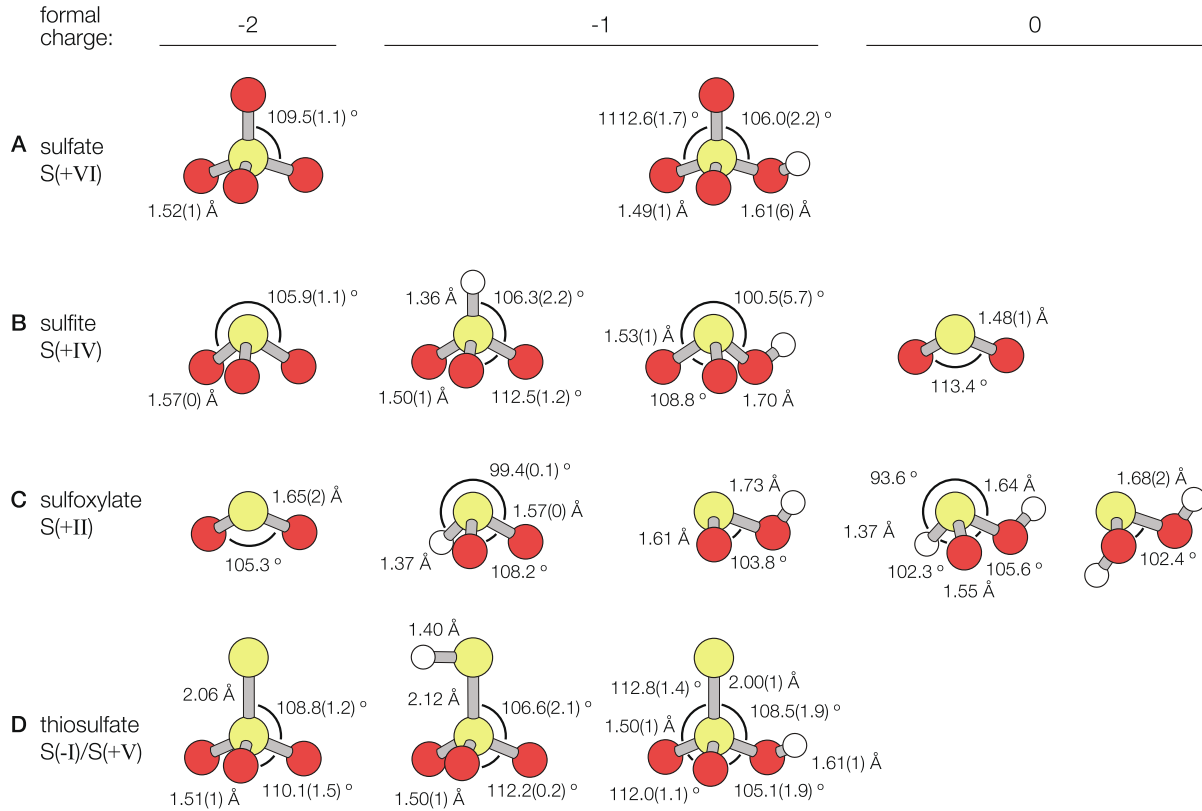


Fig. 1. Ball-and-stick representation of all sulfoxyanion species. Species are separated by sulfur redox state: (A) sulfate species, S(+VI): SO_4^{2-} and $\text{SO}_3(\text{OH})^-$; (B) sulfite species, S(+IV): SO_3^{2-} , $(\text{HS})\text{O}_3^-$, $\text{SO}_2(\text{OH})^-$, and $\text{SO}_{2(\text{aq})}$; (C) sulfoxylate species, S(+II): SO_2^{2-} , $(\text{HS})\text{O}_2^-$, $\text{SO}(\text{OH})^-$, $(\text{HS})\text{O}(\text{OH})$, and $\text{S}(\text{OH})_2$; and (D) thiosulfate species, mixed valence [S(-I) sulfanyl and S(+V) sulfonate]: $\text{S}_2\text{O}_3^{2-}$, $(\text{HS})\text{SO}_3^-$, and $\text{S}_2\text{O}_2(\text{OH})^-$. Reported bond lengths and angles refer to those calculated for a $30 \cdot \text{H}_2\text{O}$ water droplet cluster using the B3LYP/6-31+G(d,p) method (-OH bond lengths and angles are not shown but are included in Table S3); water molecules are omitted for visual clarity. Atom colors refer to: yellow = sulfur, red = oxygen, white = hydrogen.

international reference standard. Here we report results in units of “permil” (‰) by multiplying Eq. 1 by 1000. For any fractionation process (kinetic or equilibrium), the oxygen-isotope composition of product “A” and reactant “B” are related by the fractionation factor:

$$^*\alpha_{A/B} = \frac{^*\text{R}_A}{^*\text{R}_B} \quad (2)$$

While not explicitly stated here for notational convenience, all equilibrium fractionation is temperature dependent. When considering all three oxygen isotopes, $^{18}\alpha_{A/B}$ and $^{17}\alpha_{A/B}$ are related by the mass law for a given process:

$$^{17}\theta_{A/B} = \frac{\ln ^{17}\alpha_{A/B}}{\ln ^{18}\alpha_{A/B}} \quad (3)$$

Although each process is described by a unique mass law, fractionation is deemed “mass dependent” if $^{17}\theta \approx 1/2$ (i.e., since the mass difference between ^{17}O and ^{16}O is approximately half of that between ^{18}O and ^{16}O). To quantify small deviations from the expected mass-dependent $\delta^{17}\text{O}$ – $\delta^{18}\text{O}$ relationship, we let

$$\Delta'^{17}\text{O}_A = \ln(\delta^{17}\text{O}_A + 1) - ^{17}\theta_{\text{RL}} \ln(\delta^{18}\text{O}_A + 1), \quad (4)$$

where $^{17}\theta_{\text{RL}}$ is the mass law for the “reference line” and prime (\prime) indicates the use of logarithmic $\delta^*\text{O}$ values. Like $\delta^*\text{O}_A$, here we report $\Delta'^{17}\text{O}_A$ in units of permil by multiplying Eq. 4 by 1000. Although the choice of reference line is arbitrary, here we set $^{17}\theta_{\text{RL}} = 0.5305$ since this corresponds to the high-temperature limit of equilibrium fractionation; i.e., the ratio of reduced masses between isotopes of atomic oxygen (Young et al., 2002). Finally,

the temperature-dependent $\Delta'^{17}\text{O}$ offset between product “A” and reactant “B” for any fractionation process is defined as

$$\begin{aligned} \Delta\Delta'^{17}\text{O}_{A/B} &= \Delta'^{17}\text{O}_A - \Delta'^{17}\text{O}_B \\ &= [^{17}\theta_{A/B} - ^{17}\theta_{\text{RL}}] \ln ^{18}\alpha_{A/B}. \end{aligned} \quad (5)$$

Our goal is to theoretically estimate $^{18}\alpha_{A/\text{H}_2\text{O}(\text{liq})}$ and $\Delta\Delta'^{17}\text{O}_{A/\text{H}_2\text{O}(\text{liq})}$ over a range of environmentally relevant temperatures, where “A” is any sulfoxyanion species of interest.

2.2. The Bigeleisen–Goeppert Mayer–Urey equation

To estimate fractionation factors, we utilize the Bigeleisen–Goeppert Mayer–Urey (B-GM-U) equation, which predicts the equilibrium constant of isotope substitution using translational, rotational, and vibrational reduced partition function ratios (RPFs) for each isotopologue of a given molecule (Bigeleisen and Goeppert, 1947; Urey, 1947). It is subject to four main approximations: (i) a molecule’s rotational motion can be treated as a rigid rotor, (ii) its vibrational motion can be treated as a harmonic oscillator, (iii) the motion of electrons and nuclei are decoupled such that isotopic substitution has no effect on electronic potential energy surface and molecular structure (the so-called Born–Oppenheimer approximation; Born and Oppenheimer, 1927), and (iv) the ratio of the moments of inertia of two isotopically substituted molecules depends only on their masses and the product of their vibrational frequency ratios (the so-called Teller–Redlich product rule; Redlich, 1935; Wilson et al., 1955).

By following these approximations and utilizing a statistical mechanical treatment of molecular motion the B-GM-U equation can be written as:

$${}^*RPF\text{R}_h = \prod_{i=1}^{3n-x} \left(\frac{u_i^*}{u_i} \right)_{\text{TR}} \left(\frac{e^{-u_i^*/2}}{e^{-u_i/2}} \right)_{\text{ZPE}} \left(\frac{1 - e^{-u_i}}{1 - e^{-u_i^*}} \right)_{\text{EXC}}, \quad (6)$$

where

$$u_i = \frac{hc\omega_i}{k_B T}, \quad (7)$$

h is Planck’s constant, c is the speed of light, ω_i is the harmonic normal mode frequency for degree-of-freedom i , k_B is Boltzmann’s constant, T is temperature in Kelvin, n is the number of atoms in the compound of interest, and $x = 5$ for linear molecules or $x = 6$ for nonlinear molecules. As above, “*” denotes terms related to the compound containing the heavy isotope, whereas the subscript “h” indicates the pure harmonic approximation result. We have amended Eq. 6 with the subscripts “TR”, “ZPE”, and “EXC” to denote contributions from partition functions for translation/rotation, zero-point energy of vibration, and excited vibrational states, respectively.

To tabulate fractionation factors for molecules containing several non-equivalent isotopically substitutable atoms (as is the case for oxygen atoms in sulfoxyanions considered here), [Richet et al. \(1977\)](#) defined the ${}^*\beta$ factor, which represents bulk isotope fractionation between the molecule of interest and an idealized mono-atomic, non-interacting gas (e.g., an O atom). Ignoring multiply substituted isotopologues, ${}^*\beta$ can be approximated as the geometric mean of the RPFs for all singly-substituted isotopomers of a given molecule:

$${}^*\beta \approx \left(\prod_{i=1}^m {}^*RPF\text{R}_i \right)^{1/m}, \quad (8)$$

where m is the number of atoms of the element of interest (e.g., oxygen) contained within the molecule (e.g., [Richet et al., 1977](#); [Liu et al., 2010](#)). Eq. 8 states that ${}^*\beta \approx {}^*RPF\text{R}$ only for the special case where all isotopically substitutable atoms are equivalent (e.g., oxygen-isotope substitution in symmetric sulfox gases; [Fig. S1](#)). Oxygen-18 fractionation between two compounds “A” and “B” can then be written as the ratio of their ${}^{18}\beta$ values:

$${}^{18}\alpha_{A/B} = \frac{{}^{18}\beta_A}{{}^{18}\beta_B}. \quad (9)$$

Following [Cao and Liu \(2011\)](#), we extend this nomenclature for all three oxygen isotopes by defining:

$${}^{17}\kappa = \frac{\ln {}^{17}\beta}{\ln {}^{18}\beta}, \quad (10)$$

which similarly represents the equilibrium mass law between the compound of interest and an idealized, mono-atomic, non-interacting O atom. For any compound of interest, it follows that

$$\lim_{T \rightarrow \infty} {}^{17}\kappa = \frac{\left(\frac{1}{{}^{16}\text{M}} - \frac{1}{{}^{17}\text{M}} \right)}{\left(\frac{1}{{}^{16}\text{M}} - \frac{1}{{}^{18}\text{M}} \right)} = 0.5305, \quad (11)$$

where ${}^{16}\text{M}$, ${}^{17}\text{M}$, and ${}^{18}\text{M}$ are the atomic masses of ${}^{16}\text{O}$, ${}^{17}\text{O}$, and ${}^{18}\text{O}$ (see [Matsuhisa et al., 1978](#); [Young et al., 2002](#), for derivation). That is, ${}^{17}\kappa$ should approach the high-temperature limit of equilibrium fractionation. Combining Eqs. 3, 9, and 10, the mass law for equilibrium fractionation between two compounds “A” and “B” can be written as a function of their ${}^{18}\beta$ and ${}^{17}\kappa$ values:

$${}^{17}\theta_{A/B} = {}^{17}\kappa_A + ({}^{17}\kappa_A - {}^{17}\kappa_B) \left(\frac{\ln {}^{18}\beta_B}{\ln {}^{18}\beta_A - \ln {}^{18}\beta_B} \right). \quad (12)$$

Similar to previous studies (e.g., [Cao and Liu, 2011](#); [Hayles et al., 2018](#); [Schauble and Young, 2021](#)), we report all results as ${}^{18}\beta$ and ${}^{17}\kappa$ rather than reporting ${}^{18}\alpha_{A/B}$ and ${}^{17}\theta_{A/B}$ directly.

2.3. Corrections to the B-GM-U equation

The approximations required to derive the B-GM-U equation can lead to large deviations between predicted and experimental equilibrium fractionation factors; several studies have thus proposed RPF correction terms to reduce this inaccuracy (e.g., [Richet et al., 1977](#); [Liu et al., 2010](#); [Zhang and Liu, 2018](#); [Schauble and Young, 2021](#)). Theoretical corrections generally fall into one of three categories: (i) deviations from the rigid rotor approximation, including quantum mechanical rotation corrections, centrifugal distortion, and torsion effects ([Liu et al., 2010](#)); (ii) deviations from the harmonic oscillator approximation, including anharmonic vibrational energy-state corrections and double-well potentials ([Liu et al., 2010](#); [Schauble and Young, 2021](#)); and (iii) coupling, including vibration–rotation coupling and electron–nuclear coupling (i.e., deviations from the Born–Oppenheimer approximation; [Born and Huang, 1954](#); [Liu et al., 2010](#); [Zhang and Liu, 2018](#)).

As has been done previously, we ignore corrections of categories (i) and (iii) throughout this study. Specifically, [Liu et al. \(2010\)](#) have shown using a suite of gaseous compounds that all deviations from the rigid rotor approximation for rotational RPFs, as well as vibration–rotation coupling, negligibly impact ${}^*\beta$ estimates for non-hydrogen elements, including oxygen. Similarly, while inaccuracies due to deviations from the Born–Oppenheimer approximation can become significant at ultra-cold temperatures and for hydrogen-isotope fractionation, their impacts on ${}^{18}\beta$ and ${}^{17}\beta$ are likely small at temperatures relevant to Earth-surface conditions. For example, [Zhang and Liu \(2018\)](#) predict that the Born–Oppenheimer approximation leads to an over-estimate of ${}^{18}\alpha$ between gas-phase H_2O and SO_3 of 1.7‰ at -25°C and that this offset decreases with increasing temperature. While not negligible, this inaccuracy is well within the experimental ${}^{18}\alpha$ uncertainty for many species studied here (cf., [Lloyd, 1968](#); [Chiba et al., 1981](#); [Müller et al., 2013a](#); [Wankel et al., 2014](#), this study).

For category (ii) errors, [Liu et al. \(2010\)](#) predict that anharmonic corrections to the zero-point energy (ZPE) of vibration may exhibit an appreciable impact on ${}^*RPF\text{R}$ and thus ${}^*\beta$ estimates for non-hydrogen elements, whereas anharmonic corrections to excited vibrational states do not. Furthermore, [Schauble and Young \(2021\)](#) recently concluded that double-well vibrational potentials—which are present in hydrogen-bonding solutions such as water—do not influence $\Delta^{17}\text{O}$ by more than 0.01‰. We therefore ignore corrections for anharmonic excited states and double-well potentials, but we do estimate anharmonic ZPE effects for gaseous species using a modified B-GM-U equation. Specifically, if the anharmonic ZPE can be quantified directly, then the ZPE partition functions can be removed from the RPF product and Eq. 6 can be rewritten as

$${}^*RPF\text{R}_{\text{AnZPE}} = \left(\frac{e^{-z^*}}{e^{-z}} \right)_{\text{ZPE}} \prod_{i=1}^{3n-x} \left(\frac{u_i^*}{u_i} \right)_{\text{TR}} \left(\frac{1 - e^{-u_i}}{1 - e^{-u_i^*}} \right)_{\text{EXC}}, \quad (13)$$

where

$$z = \frac{hc\zeta}{k_B T}, \quad (14)$$

ζ is the total ZPE (including harmonic and anharmonic contributions), and the subscript “AnZPE” indicates that the result includes anharmonic ZPE corrections. Combining Eq. 6 and 13 yields

$${}^* \text{RPFR}_{\text{AnZPE}} = ({}^* \text{AnZPE})({}^* \text{RPFR}_{\text{h}}), \quad (15)$$

where

$${}^* \text{AnZPE} = \frac{\left(\frac{e^{-z^*}}{e^{-\sum u_i^*/2}} \right)}{\left(\frac{e^{-z}}{e^{-\sum u_i/2}} \right)} \quad (16)$$

is the anharmonic correction to the ZPE partition function ratio following the nomenclature of Liu et al. (2010).

In practice, direct determination of ζ values for aqueous sulfoxyanions is not feasible due to computational constraints, whereas empirical ZPE correction factors likely carry prohibitively large bias and uncertainty (e.g., Irikura et al., 2009). Following current best practice (e.g., Liu et al., 2010; Eldridge et al., 2016; Liu and Liu, 2016), we therefore instead qualitatively assess the impact of anharmonicity in Section 4.1 using ZPEs determined for ideal gaseous (“*in vacuo*”) sulfoxy species with and without anharmonic corrections. We specifically calculate ${}^* \text{AnZPE}$ for a suite of sulfoxy gases (Fig. S1) using Eq. 16 and discuss the likely magnitude of anharmonic ZPE corrections on aqueous sulfoxyanions in light of these results.

2.4. Potential energy surface corrections

Computational constraints require that methods with a less accurate potential energy surface (PES) are used when analyzing large molecules—including explicitly solvated anions—resulting in ω values that are systematically biased (Irikura et al., 2005). These biases can be partially corrected by empirically scaling sulfoxyanion ω values to those determined using highly accurate PES methods (e.g., Scott and Radom, 1996; Merrick et al., 2007).¹ Here, we calculate PES scaling factors as the ratio of ω values for gaseous sulfoxy species determined using several computational theories and basis sets; we report all scaled results with the subscript “Sc”. An analogous approach was used in a previous theoretical estimate of ^{18}O fractionation between SO_4^{2-} and water; it was shown to reduce the misfit between theoretical experimental results by several permil, highlighting the utility of PES scaling factors when determining $^{18}\beta$ values (Zeebe, 2010).²

Finally, because ω and ZPE values are related to electron density, it is reasonable to hypothesize that correction factors depend on sulfur-atom(s) redox state(s). This hypothesis is supported by Eldridge et al. (2016), who observed a larger anharmonic ZPE correction for *in vacuo* species in the S(+VI) redox state relative to more reduced species. As detailed in Sections 3 and 4, we therefore explore the effect of redox-specific PES scaling factors on resulting ${}^* \beta_{\text{h,Sc}}$ values for aqueous sulfoxyanions.

3. Methods

Descriptions of the experimental methods for all sulfite-water and thiosulfate-water equilibrium experiments included as part of this study are reported in the Supplementary Material. All ZPEs and harmonic frequencies were estimated using the computational

¹ This differs from the common practice of scaling harmonic to fundamental frequencies, which are inappropriate for the B-GM-U equation (see Liu et al., 2010, for details).

² However, the scaling factors used in Zeebe (2010) appear to compare his calculated harmonic frequencies to experimental fundamental frequencies from Pye and Rudolph (2001), which would be inconsistent with B-GM-U equation best practice (see Liu et al., 2010, for details).

chemistry software Gaussian 16 on the Research Computing cluster at Harvard University (Frisch et al., 2016). For all species, geometry optimizations were performed first, followed by isotope-specific frequency calculations. The masses of all atoms other than the oxygen atom of interest were assumed to equal their respective major isotopes (i.e., ^1H , ^{16}O , and ^{32}S). For species with several possible isotopomers (e.g., isotopic substitution at each O atom in SO_4^{2-}), frequencies and RPFs were calculated individually for each isotopomer, and resulting ${}^* \beta$ values were subsequently calculated using Eq. 8. After each step, convergence was ensured by confirming that stationary points were found (i.e., that no imaginary frequencies exist).

All optimization and frequency calculations were performed using one of three methods of varying accuracy: (i) B3LYP/6-31+G(d,p) (Lee et al., 1988; Becke, 1993), (ii) CCSD/aug-cc-pVTZ (Scuseria et al., 1988; Kendall et al., 1992), and (iii) MP2/aug-cc-pVTZ (Møller and Plesset, 1934; Frisch et al., 1990; Kendall et al., 1992). Method (i) is a low/moderate-complexity hybrid of Hartree-Fock (HF) and density functional theory (DFT) with a double-zeta Pople basis set, including diffuse and polarization functions. It has been used previously to estimate multiple-sulfur isotope fractionation factors of sulfoxyanions and polysulfur compounds (Eldridge et al., 2016; Eldridge et al., 2021); similar methods have additionally been used to estimate triple-oxygen isotope fractionation factors for a range of gaseous, aqueous, and mineral species (Cao and Liu, 2011; Hill et al., 2014; Hayles et al., 2018; Guo and Zhou, 2019). Here, we applied method (i) to all gaseous and aqueous species, including anharmonic ZPE corrections for gaseous species. Method (ii) is a high-complexity coupled cluster HF theory with a correlation-consistent polarized triple-zeta basis set, augmented with diffuse functions. It is a highly accurate but computationally expensive method and was used here for gaseous species to estimate the effect of basis-set accuracy on fractionation factor results (i.e., to calculate PES scaling factors). Method (iii) utilizes second-order Møller-Plesset perturbation theory with the same basis set used in method (ii). Like method (ii), it is accurate yet computationally expensive; however, unlike method (ii), it additionally allows for anharmonic corrections because the analytic second derivatives can be calculated (Frisch et al., 1990; Frisch et al., 2016). This method was used here for gaseous species to estimate the effect of basis-set accuracy as well as anharmonic ZPE corrections on fractionation factor results (i.e., to calculate PES scaling factors and estimate the impact of ZPE anharmonicity), as has been done previously (Liu et al., 2010).

3.1. Gaseous species computations

To calculate PES scaling factors and evaluate anharmonic ZPE corrections and their effect on isotope fractionation-factor estimates, several gaseous sulfoxy species of varying sulfur redox states were analyzed: (i) $\text{SO}_{3(\text{g})}$ [S(+VI)], (ii) $\text{SO}_{2(\text{g})}$ [S(+IV)], (iii) $\text{S}_2\text{O}_{2(\text{g})}$ and $\text{SO}_{(\text{g})}$ [S(+II)], (iv) $\text{S}_{3(\text{g})}$ and $\text{S}_{2(\text{g})}$ [S(0), elemental], (v) $\text{H}_2\text{S}_{(\text{g})}$ [S(-II)], (vi) (S) $\text{SO}_{2(\text{g})}$ [mixed valence S(-I)/S(+V)]; water vapor, $\text{H}_2\text{O}_{(\text{vap.})}$, and molecular oxygen, $\text{O}_{2(\text{g})}$, were additionally analyzed (Fig. S1). Harmonic frequencies and ZPEs for all gaseous species were calculated using all three methods, and anharmonic ZPEs were calculated using B3LYP/6-31+G(d,p) and MP2/aug-cc-pVTZ methods.

We note that the atom-specific formal oxidation states of (S) $\text{SO}_{2(\text{g})}$ are assumed by comparison to aqueous thiosulfate (Vairavamurthy et al., 1993) and have not been determined experimentally. Similarly, the physical-chemical relationship between gas-phase (S) $\text{SO}_{2(\text{g})}$ and aqueous-phase thiosulfate species has not been demonstrated directly. Rather, this is inferred based on theoretical results and by analogy to the known relationship between

sulfate species and $\text{SO}_{3(\text{g})}$ (e.g., Marsden and Smith, 1990; Clements et al., 2002; Ramírez-Solís et al., 2011; Hochlaf et al., 2021).

3.2. Liquid water computations

To obtain $^{17}\kappa$ estimates, liquid water harmonic frequencies were calculated following the procedure of Hayles et al. (2018) using the B3LYP/6-31+G(d,p) method. First, water “droplets” were generated by starting with 6 H_2O molecules and iteratively performing a geometry optimization followed by the addition of 4 more H_2O molecules until a final cluster size of 30 H_2O molecules was achieved. Such iterative optimizations are commonly performed to ensure that water droplet geometry remains stable (e.g., Li et al., 2009; Zeebe, 2010; Li and Liu, 2011; Eldridge et al., 2016). Then, each H_2O molecule was individually isotopically substituted and harmonic frequencies were determined, yielding $n = 30$ sets of frequencies. Finally, to minimize the influence of water droplet cluster geometry on resulting $^*\beta$ values, the whole procedure was repeated 4 more times with arbitrary molecular geometries for a total of $n = 5$ water droplets.

3.3. Aqueous sulfoxyanion computations

Aqueous sulfoxyanion harmonic frequencies were calculated following the procedure of Eldridge et al. (2016) using the B3LYP/6-31+G(d,p) method. Several species at each redox state were considered: (i) SO_4^{2-} and $\text{SO}_3(\text{OH})^-$ [S(+VI), collectively termed “sulfate species”]; (ii) SO_3^{2-} , $(\text{HS})\text{O}_3^-$, $\text{SO}_2(\text{OH})^-$, and dissolved $\text{SO}_{2(\text{aq})}$ gas [S(+IV), collectively termed “sulfite species”]; (iii) SO_2^{2-} , $(\text{HS})\text{O}_2^-$, $\text{SO}(\text{OH})^-$, $(\text{HS})\text{O}(\text{OH})$, and $\text{S}(\text{OH})_2$ [S(+II), collectively termed “sulfoxylate species”]; and finally (iv) $\text{S}_2\text{O}_3^{2-}$, $(\text{HS})\text{SO}_3^-$, and $\text{S}_2\text{O}_2(\text{OH})^-$ [mixed valence S(-I)/S(+V), collectively termed “thio-sulfate species”] (Fig. 1). Like liquid water calculations, all sulfoxyanions were analyzed using the water “droplet” method (Li et al., 2009; Li and Liu, 2011). Droplets were generated by starting with the sulfoxyanion of interest and 6 H_2O molecules; geometry optimizations and subsequent H_2O additions were performed until a final cluster size of $n = 30$ H_2O molecules was reached. Special care was taken to monitor sulfoxyanion -OH bond lengths, as geometric instabilities could lead to deprotonation, particularly for highly acidic species. To estimate isotope fractionation uncertainty resulting from droplet geometry and stretched -OH bonds, both $\text{SO}_3(\text{OH})^-$ and $\text{S}_2\text{O}_2(\text{OH})^-$ water droplet geometries were determined in triplicate.

3.4. Sources of uncertainty and statistical methods

There exist three main potential sources of uncertainty and/or bias: (i) assumptions required to derive the B-GM-U equation (Section 2.2–2.3); (ii) approximations inherent to the particular computational theory and basis set used to model the molecular PES, including scaling factor uncertainty (Section 2.4); and (iii) variability due to water droplet geometry, for example due to the importance of water dimers and trimers at higher temperature (Eldridge et al., 2016; Hayles et al., 2018). To assess points (i) and (ii), we empirically calculate PES scaling factors and estimate possible bias arising from ZPE anharmonicity for a suite of gaseous sulfoxyl compounds using several theories and basis sets (e.g., following Liu et al., 2010; Cao and Liu, 2011). To assess point (iii), we determine triplicate water droplet geometries for a subset of sulfoxyanion species [$\text{SO}_3(\text{OH})^-$ and $\text{S}_2\text{O}_2(\text{OH})^-$]. We additionally calculate semi-empirical liquid water $^*\beta$ values following the method of Hayles et al. (2018) since theoretical results may not fully capture liquid water molecular interactions.

Finally, we assess the overall accuracy of our results by comparing predicted $^{18}\alpha_{\text{A}/\text{H}_2\text{O}(\text{liq})}$ with all existing theoretical and experimental results from the literature, where “A” is the sulfoxyanion of interest (Lloyd, 1968; Chiba et al., 1981; Zeebe, 2010; Müller et al., 2013a; Wankel et al., 2014, this study). Unfortunately, no experimental equilibrium $\Delta\Delta' ^{17}\text{O}_{\text{A}/\text{H}_2\text{O}(\text{liq})}$ estimates currently exist for sulfoxyanions. However, as mentioned previously, theoretical $\Delta\Delta' ^{17}\text{O}_{\text{A}/\text{H}_2\text{O}(\text{liq})}$ error has been shown to be small—even if $^{18}\alpha_{\text{A}/\text{H}_2\text{O}(\text{liq})}$ is in error by several permil—due to mass-dependent error cancellation (Cao and Liu, 2012). We therefore assume that theoretical $\Delta\Delta' ^{17}\text{O}_{\text{A}/\text{H}_2\text{O}(\text{liq})}$ predictions are accurate if the corresponding $^{18}\alpha_{\text{A}/\text{H}_2\text{O}(\text{liq})}$ agrees with experimental results to within several permil.

All regressions (e.g., when calculating PES scaling factors) were performed using orthogonal distance regression, which allows for uncertainty in both x and y variables. Regression results are reported with $\pm 1\sigma$ uncertainty. Statistical differences between populations were determined using a two-way analysis of variance (ANOVA) and evaluated at the $p = 0.05$ level. Misfit between theoretical predictions and experimental results was determined as the root mean square error (RMSE); to estimate bulk solution fractionation for each experiment, “mean” fractionation factors were calculated as the average of all species (including isomers where appropriate) weighted by their pH-specific relative abundance (see Millero et al., 1989; Eldridge et al., 2018, for speciation constants used here).

4. Results and interpretation

Detailed descriptions of the experimental results for all sulfite-water and thiosulfate-water equilibrium experiments included as part of this study are reported in the Supplementary Material. Predicted bond lengths and angles for all gaseous species using all methods are reported in Table S1, whereas calculated ZPEs and harmonic frequencies are reported in Table S2. Similarly, predicted bond lengths and angles for aqueous sulfoxyanions are reported in Table S3, whereas ZPEs and harmonic frequencies are reported in Table S4. All optimization and frequency results, as well as python scripts used to calculate all $^*\text{RPF}$, $^*\beta$, $^{17}\kappa$, $^{18}\alpha$ and $\Delta' ^{17}\text{O}$ values, are included in the Supplementary Data. Finally, following common practice, seventh-order polynomial fits for calculating $^{18}\beta_{\text{h,sc}}$ and $^{17}\kappa_{\text{h,sc}}$ for $\text{H}_2\text{O}_{(\text{vap})}$, $\text{H}_2\text{O}_{(\text{liq})}$, $\text{O}_{2(\text{g})}$, $\text{O}_{2(\text{aq})}$, and all sulfoxyanions of interest as a function of temperature are reported in Tables 1 and 2.

4.1. Gaseous species and scaling factors

For gaseous species, all methods result in similar optimized geometries with slight differences in bond lengths and angles. Bond length differences between methods reach a maximum of 0.12Å (for S-S in $\text{S}_2\text{O}_{2(\text{g})}$) and average 0.03Å , with MP2/aug-cc-pVTZ consistently predicting the longest bonds and CCSD/aug-cc-pVTZ consistently predicting the shortest bonds. Bond angle differences between methods are similarly small, reaching a maximum of 6.1° (for O-S-S in $\text{S}_2\text{O}_{2(\text{g})}$) and averaging 1.3° with no clear trend between methods.

Here, we assess the impact of PES scaling and anharmonic ZPE correction factors and we compare all results to available experimental data. When considering all gaseous species together, ω values predicted by the CCSD/aug-cc-pVTZ method are nearly identical to experimental results for all compounds reported in Johnson (2020), with an experimental vs. theoretical regression slope of 1.0062 ± 0.0002 ($r^2 = 0.9999$; Fig. S2A). Similarly, ω predictions using the MP2/aug-cc-pVTZ method are generally nearly identical to experimental values (noting that experimental ω val-

Table 1
Seventh-order polynomial fit parameters to the equation: $\ln(^{18}\beta_{h,sc}) = \sum_{i=0}^7 \frac{p[i]}{T^i}$, where T is in Kelvin. n.a. = not applicable; RMSE = root mean square error between “true” values and polynomial fits; redox = sulfur atom redox state. Polynomial fits were determined over the temperature range 0 °C to 375 °C. All results are calculated using B3LYP/6-31+G(d,p) harmonic frequencies scaled to redox state-specific CCSD/aug-cc-pVTZ harmonic frequencies (Section 3).

Compound	Redox	Solvation	p[7]	p[6]	p[5]	p[4]	p[3]	p[2]	p[1]	p[0]	RMSE
SO ₄ ²⁻	S(+VI)	30-H ₂ O	8.78601E+14	-1.95731E+13	1.78992E+11	-7.77749E+08	6.55636E+05	1.04820E+04	3.65001E-01	-8.62190E-05	4.43E-10
^a SO ₃ (OH) ⁻	S(+VI)	30-H ₂ O	8.38462E+14	-1.76125E+13	1.47718E+11	-5.32648E+08	-3.78406E+05	1.25845E+04	1.43947E-01	-4.80939E-05	7.23E-10
SO ₃ ²⁻	S(+IV)	30-H ₂ O	3.66629E+14	-9.30106E+12	9.66757E+10	-4.76445E+08	4.66763E+05	7.99128E+03	3.84315E-01	-1.08687E-04	1.97E-10
(HS)O ₃ ⁻	S(+IV)	30-H ₂ O	1.24473E+15	-2.64675E+13	2.28627E+11	-9.23583E+08	6.66919E+05	1.07948E+04	2.07897E-01	-2.60006E-05	1.05E-09
SO ₂ (OH) ⁻	S(+IV)	30-H ₂ O	6.82041E+13	-2.92554E+12	3.52829E+10	-1.29354E+08	-7.39006E+05	1.02126E+04	1.10153E+00	-4.39195E-04	1.54E-09
SO ₂ (aq.)	S(+IV)	30-H ₂ O	1.71412E+15	-3.45618E+13	2.78591E+11	-1.01405E+09	3.82197E+05	1.14887E+04	-2.92787E-01	1.43303E-04	2.26E-09
SO ₂ ²⁻	S(II)	30-H ₂ O	1.07018E+14	-3.41895E+12	4.23219E+10	-2.35750E+08	1.43012E+05	6.62551E+03	2.10169E-01	-6.71941E-05	2.33E-10
(HS)O ₂ ⁻	S(II)	30-H ₂ O	5.06763E+14	-1.21919E+13	1.20053E+11	-5.60229E+08	5.57702E+05	7.79056E+03	4.01088E-01	-1.09030E-04	1.14E-10
SO(OH) ⁻	S(II)	30-H ₂ O	-3.78227E+14	6.35998E+12	-4.38641E+10	2.00762E+08	-1.22257E+06	8.93166E+03	2.20550E+00	-8.23579E-04	2.35E-09
(HS)O(OH)	S(II)	30-H ₂ O	-2.00354E+14	2.82582E+12	-1.82261E+10	1.52296E+08	-1.62504E+06	1.16209E+04	8.04313E-01	-4.00558E-04	2.00E-09
S(OH) ₂	S(II)	30-H ₂ O	-1.13930E+15	2.20537E+13	-1.83002E+11	8.88544E+08	-3.26057E+06	1.23554E+04	2.93683E+00	-1.21589E-03	4.52E-09
S ₂ O ₃ ²⁻	S(-I)/S(+V)	30-H ₂ O	1.03690E+15	-2.25218E+13	1.99790E+11	-8.36775E+08	6.63717E+05	1.05965E+04	2.95242E-01	-5.92284E-05	7.05E-10
(HS)SO ₃ ⁻	S(-I)/S(+V)	30-H ₂ O	1.28715E+15	-2.70326E+13	2.30223E+11	-9.12621E+08	5.75406E+05	1.12567E+04	8.41668E-02	1.40096E-05	1.26E-09
^a S ₂ O ₂ (OH) ⁻	S(-I)/S(+V)	30-H ₂ O	4.64300E+14	-1.00106E+13	8.28086E+10	-2.39042E+08	-1.07055E+06	1.31562E+04	-4.77777E-01	9.16434E-05	9.43E-11
O ₂ (aq.)	n.a.	30-H ₂ O	1.68656E+15	-2.65569E+13	1.27979E+11	1.71347E+08	-4.26222E+06	1.89319E+04	-4.95549E+00	1.54667E-03	7.11E-09
O ₂ (g)	n.a.	0-H ₂ O	1.42416E+15	-1.98429E+13	5.54305E+10	5.98686E+08	-5.71917E+06	2.13767E+04	-6.24658E+00	1.91698E-03	7.80E-09
H ₂ O(liq.)	n.a.	30-H ₂ O	-2.08862E+15	4.25765E+13	-3.75880E+11	1.88200E+09	-5.91132E+06	1.29812E+04	7.88716E+00	-2.95069E-03	7.65E-09
^b H ₂ O(liq.)	n.a.	30-H ₂ O	-1.43935E+15	2.94746E+13	-2.63299E+11	1.34665E+09	-3.98119E+06	7.27847E+03	1.79311E+01	-1.14770E-02	6.18E-09
^c H ₂ O(liq.)	n.a.	30-H ₂ O	-3.45950E+16	6.90085E+14	-5.90267E+12	2.81504E+10	-8.08683E+07	1.41111E+05	-1.14006E+02	4.60253E-02	1.46E-07
H ₂ O(vap.)	n.a.	0-H ₂ O	-1.43935E+15	2.94746E+13	-2.63299E+11	1.34665E+09	-4.33160E+06	8.94247E+03	1.12188E+01	-3.79195E-03	6.18E-09

^aaverage of repeat optimizations ($n = 3$).

^bfreshwater; semi-empirical using $^{18}\alpha_{liq./vap.}$ from Horita et al. (2008) (their Eq. 20).

^c4 M NaCl; semi-empirical semi-empirical using $^{18}\alpha_{liq./vap.}$ from Horita et al. (1995) (their Eq. 10).

Table 2

Seventh-order polynomial fit parameters to the equation: ${}^{17}k_{h,sc} = \sum \frac{p[i]}{T^i}$, where T is in Kelvin. n.a. = not applicable; RMSE = root mean square error between “true” values and polynomial fits; redox = sulfur atom redox state. Polynomial fits were determined over the temperature range 0 °C to 375 °C. All results are calculated using B3LYP/6-31+G(d,p) harmonic frequencies scaled to redox state-specific CCSD/aug-cc-pVTZ harmonic frequencies (Section 3).

Compound	Redox	Solvation	p[7]	p[6]	p[5]	p[4]	p[3]	p[2]	p[1]	p[0]	RMSE
SO ₄ ²⁻	S(+VI)	30-H ₂ O	-1.09758E+14	2.21141E+12	-1.78053E+10	6.57357E+07	-5.66693E+04	-2.99476E+02	9.26814E-02	5.30382E-01	1.77E-10
^a SO ₃ (OH) ⁻	S(+VI)	30-H ₂ O	-1.05077E+14	2.08099E+12	-1.62630E+10	5.63960E+07	-3.05433E+04	-3.02550E+02	-2.79116E-02	5.30525E-01	1.41E-10
SO ₃ ²⁻	S(+IV)	30-H ₂ O	-3.96234E+13	9.13920E+11	-8.48462E+09	3.67551E+07	-4.46357E+04	-1.69421E+02	-4.27180E-02	5.30521E-01	1.17E-11
(HS)O ₃ ⁻	S(+IV)	30-H ₂ O	-1.22497E+14	2.43796E+12	-1.91137E+10	6.63946E+07	-3.78848E+04	-3.36767E+02	5.01536E-03	5.30516E-01	1.44E-10
SO ₂ (OH) ⁻	S(+IV)	30-H ₂ O	-6.64901E+13	1.47811E+12	-1.33717E+10	5.92788E+07	-1.07070E+05	-4.18025E+01	-2.40288E-01	5.30622E-01	6.37E-11
SO ₂ (aq.)	S(+IV)	30-H ₂ O	-1.80695E+14	3.41886E+12	-2.49521E+10	7.56554E+07	5.00571E+03	-5.05706E+02	7.83978E-02	5.30485E-01	3.10E-10
SO ₂ ²⁻	S(II)	30-H ₂ O	-1.25316E+13	3.46965E+11	-3.76524E+09	1.84814E+07	-2.12544E+04	-1.39015E+02	-3.05447E-02	5.30539E-01	2.05E-11
(HS)O ₂ ⁻	S(II)	30-H ₂ O	-4.78172E+13	1.08214E+12	-9.85078E+09	4.16651E+07	-4.81905E+04	-1.86465E+02	-1.66831E-02	5.30495E-01	1.06E-11
SO(OH) ⁻	S(II)	30-H ₂ O	-4.76538E+13	1.15326E+12	-1.17307E+10	6.26396E+07	-1.71944E+05	1.85461E+02	-3.92561E-01	5.30650E-01	7.50E-11
(HS)O(OH)	S(II)	30-H ₂ O	-2.60875E+13	7.04739E+11	-7.40677E+09	3.66685E+07	-6.89222E+04	-4.84422E+01	-2.36279E-01	5.30579E-01	1.46E-10
S(OH) ₂	S(II)	30-H ₂ O	3.46324E+12	1.48483E+11	-3.60663E+09	2.93649E+07	-1.07974E+05	1.67364E+02	-4.54152E-01	5.30629E-01	2.29E-10
S ₂ O ₃ ²⁻	S(-)/S(+V)	30-H ₂ O	-1.07145E+14	2.16090E+12	-1.72580E+10	6.18459E+07	-4.22008E+04	-3.08034E+02	4.70051E-03	5.30496E-01	1.17E-10
(HS)SO ₃ ⁻	S(-)/S(+V)	30-H ₂ O	-1.29541E+14	2.53963E+12	-1.95034E+10	6.51641E+07	-2.39071E+04	-3.75098E+02	1.61815E-02	5.30519E-01	1.73E-10
^a S ₂ O ₂ (OH) ⁻	S(-)/S(+V)	30-H ₂ O	-7.52210E+13	1.52470E+12	-1.20845E+10	4.10306E+07	-6.18271E+03	-3.04065E+02	-3.29340E-02	5.30523E-01	4.24E-11
O ₂ (aq.)	n.a.	30-H ₂ O	-1.02570E+14	9.71667E+11	4.75982E+09	-1.08093E+08	6.12747E+05	-1.47572E+03	6.42898E-01	5.30408E-01	8.15E-10
O ₂ (g)	n.a.	0-H ₂ O	-5.80617E+13	-8.25316E+10	1.52917E+10	-1.64857E+08	7.85862E+05	-1.75247E+03	8.04564E-01	5.30277E-01	8.86E-10
H ₂ O(liq.)	n.a.	30-H ₂ O	1.05974E+13	-5.11341E+10	-1.39684E+09	1.89828E+07	-1.08561E+05	3.48422E+02	-7.32671E-01	5.30751E-01	2.85E-10
^b H ₂ O(liq.)	n.a.	30-H ₂ O	3.18447E+14	-5.98830E+12	4.72301E+10	-1.99574E+08	4.67581E+05	-5.26600E+02	-4.54266E-02	5.30568E-01	2.06E-09
^c H ₂ O(liq.)	n.a.	30-H ₂ O	4.52795E+14	-9.03830E+12	7.69053E+10	-3.60396E+08	9.93666E+05	-1.57010E+03	1.12353E+00	5.29993E-01	1.27E-09
H ₂ O(vap.)	n.a.	0-H ₂ O	-5.70609E+13	1.29301E+12	-1.27362E+10	7.14704E+07	-2.52163E+05	5.84609E+02	-9.02390E-01	5.30787E-01	1.02E-10

^aaverage of repeat optimizations ($n = 3$).

^bfreshwater; semi-empirical using ${}^{18}\alpha_{liq./vap.}$ from Horita et al. (2008) (their Eq. 20).

^c4 M NaCl; semi-empirical semi-empirical using ${}^{18}\alpha_{liq./vap.}$ from Horita et al. (1995) (their Eq. 10).

ues are derived from observed fundamental frequencies based on a physical model; e.g., Irikura, 2007). However, all diatomic molecules (SO , S_2 , and O_2) deviate significantly from this trend, with predicted values consistently lower than experimental results. Omitting the diatomic compounds, this method yields an experimental vs. theoretical regression slope of 1.0016 ± 0.0002 ($r^2 = 0.9992$; Fig. S2B). Both methods yield slightly higher ω values than those predicted by the B3LYP/6-31+G(d,p) method, with resulting all-compound average PES scaling factors of 1.0256 ± 0.0002 for CCSD/aug-cc-pVTZ ($r^2 = 0.9991$; Fig. S2C) and 1.0173 ± 0.0002 for MP2/aug-cc-pVTZ (omitting diatomic molecules; $r^2 = 0.9992$; Fig. S2D). When separating compounds by redox state, PES scaling factors range from 1.0093 to 1.0764 for CCSD/aug-cc-pVTZ (Fig. S2E) and from 0.9840 to 1.0830 for MP2/aug-cc-pVTZ (Fig. S2F). For CCSD/aug-cc-pVTZ, scaling factors monotonically increase with increasing sulfur-atom redox state [treating mixed-valence (S) $\text{SO}_{2(\text{g})}$ as S(+V) since this is the assumed oxidation state of the O-bound sulfonate atom]. In contrast, MP2/aug-cc-pVTZ scaling factors display no such trend, with a maximum for S(0) compounds and a minimum for S(+IV) compounds.

When considering all species together, anharmonic ZPE values predicted by the B3LYP/6-31+G(d,p) and MP2/aug-cc-pVTZ methods are slightly lower than their harmonic counterparts, yielding all-compound average anharmonic ZPE regression slopes of 0.9891 ± 0.0002 ($r^2 = 1.0000$; Fig. S3A) and 0.9901 ± 0.0002 (omitting diatomic molecules; $r^2 = 0.9999$; Fig. S3B), respectively. When separated by redox state, anharmonic ZPE regression slopes range from 0.9872 to 0.9976 for B3LYP/6-31+G(d,p) (Fig. S3C) and from 0.9848 to 1.0012 for MP2/aug-cc-pVTZ (Fig. S3D). However, when only considering sulfoxy species [i.e., S(+II) through S(+VI) redox states], regression slopes are essentially identical across redox state, ranging from 0.9953 to 0.9967 for B3LYP/6-31+G(d,p) and from 0.9963 to 1.0012 for MP2/aug-cc-pVTZ. Both methods similarly predict anharmonic-corrected fundamental frequencies, ν , near the experimental values reported in Johnson (2020), yielding experimental vs. predicted regression slopes of 0.9864 ± 0.0002 for B3LYP/6-31+G(d,p) ($r^2 = 0.9993$; Fig. S4A) and 1.0020 ± 0.0002 for MP2/aug-cc-pVTZ (omitting diatomic molecules; $r^2 = 0.9993$; Fig. S4B). These are nearly identical to slopes observed previously in Liu et al. (2010). Unlike for these methods, fundamental frequencies and anharmonic ZPE corrections cannot be determined for CCSD/aug-cc-pVTZ since analytic second derivatives cannot be calculated (Scuseria et al., 1988; Frisch et al., 2016).

Resulting $^{18}\beta_{\text{h}}$ values determined using unscaled harmonic frequencies (Eq. 6) for all gaseous sulfoxy species, $\text{H}_2\text{O}_{(\text{vap.})}$, and $\text{O}_{2(\text{g})}$ are shown in Fig. S5. For all methods at a given temperature, sulfoxy species $^{18}\beta_{\text{h}}$ values generally increase with increasing sulfur redox state. For example, $^{18}\beta_{\text{h}}$ calculated at 25 °C using the B3LYP/6-31+G(d,p) method increases from 1.0738 for $\text{S}_2\text{O}_{2(\text{g})}$ to 1.0947 for $\text{SO}_{3(\text{g})}$; $\text{H}_2\text{O}_{(\text{vap.})}$ and $\text{O}_{2(\text{g})}$ predictions generally lie between those of S(+II) and S(+IV) species. For a given compound, the CCSD/aug-cc-pVTZ method predicts the highest $^{18}\beta_{\text{h}}$ at all temperatures, with B3LYP/6-31+G(d,p) and MP2/aug-cc-pVTZ both predicting lower—yet similar—values. For example, $^{18}\beta_{\text{h}}$ calculated at 25 °C for $\text{SO}_{3(\text{g})}$ ranges from 1.0947 using B3LYP/6-31+G(d,p) to 1.1065 using CCSD/aug-cc-pVTZ. For all compounds using all methods, $^{18}\beta_{\text{h}}$ values approach unity with increasing temperature, as expected (i.e., no fractionation as $T \rightarrow \infty$).

PES scaling factor corrections to B3LYP/6-31+G(d,p) results are shown in Fig. S6. When considering the all-compound average scaling factors, $^{18}\beta_{\text{h,sc}}$ values at 25 °C only differ from their unscaled counterparts by a maximum of 3.6‰ using CCSD/aug-cc-pVTZ scaling and 2.4‰ using MP2/aug-cc-pVTZ scaling [both maxima corre-

spond to $\text{SO}_{3(\text{g})}$]. In contrast, redox-state specific PES scaling factors yield $^{18}\beta_{\text{h,sc}}$ corrections at 25 °C that range from 0.7‰ [$\text{H}_2\text{O}_{(\text{vap.})}$] to 10.4‰ [$\text{SO}_{3(\text{g})}$] using CCSD/aug-cc-pVTZ and from -2.0 ‰ [$\text{SO}_{2(\text{g})}$] to 5.9‰ [(S) $\text{SO}_{2(\text{g})}$] using MP2/aug-cc-pVTZ. Interestingly, $\text{SO}_{2(\text{g})}$ scaling factors using the MP2/aug-cc-pVTZ method are consistently ≤ 1 for all T ; in contrast, all other PES scaling factors are always ≥ 1 . Like $^{18}\beta_{\text{h}}$ results, all PES scaling factors approach unity with increasing temperature.

Anharmonic ZPE corrections to $^{18}\beta_{\text{h}}$ values (Eq. 16) calculated using B3LYP/6-31+G(d,p) and MP2/aug-cc-pVTZ methods are shown in Fig. S7. All corrections range from -1.0 ‰ [$\text{O}_{2(\text{g})}$] to -0.3 ‰ [$\text{SO}_{(\text{g})}$] for B3LYP/6-31+G(d,p) and from -1.3 ‰ [$\text{O}_{2(\text{g})}$] to 0.1‰ [$\text{SO}_{(\text{g})}$] for MP2/aug-cc-pVTZ. Interestingly, S(+II) anharmonic ZPE corrections calculated using MP2/aug-cc-pVTZ are consistently ≥ 1 , unlike all other results. Similar to $^{18}\beta_{\text{h}}$ and PES scaling factor results, all anharmonic ZPE corrections approach unity with increasing temperature. Across all methods tested here, PES ω scaling factors yield consistently larger changes in $^{18}\beta$ than do AnZPE corrections; this is especially true for redox-state specific PES results. For example, the overall impact on resulting $^{18}\beta$ values of redox-state specific PES scaling factors (scaled to CCSD/aug-cc-pVTZ) and of AnZPE corrections [using B3LYP/6-31+G(d,p)] for all gaseous sulfoxy species, $\text{H}_2\text{O}_{(\text{vap.})}$, and $\text{O}_{2(\text{g})}$ are shown in Fig. S8. For all sulfoxy species, PES scaling factors yield $^{18}\beta$ corrections that are ≥ 5.8 -fold larger than those from ZPE anharmonicity at 25 °C.

Resulting $^{17}\kappa_{\text{h}}$ values calculated using unscaled harmonic frequencies (Eq. 6) for all gaseous sulfoxy species, $\text{H}_2\text{O}_{(\text{vap.})}$, and $\text{O}_{2(\text{g})}$ are shown in Fig. S9. For all methods at all temperatures, $\text{H}_2\text{O}_{(\text{vap.})}$ consistently displays the highest $^{17}\kappa_{\text{h}}$ values, whereas all other compounds cluster at lower values. For example, the B3LYP/6-31+G(d,p) method at 25 °C predicts a $^{17}\kappa_{\text{h}}$ value for $\text{H}_2\text{O}_{(\text{vap.})}$ of 0.5300 with all other compounds ranging from 0.5282 [$\text{SO}_{2(\text{g})}$] to 0.5283 [$\text{S}_2\text{O}_{2(\text{g})}$]. For all compounds and all methods, $^{17}\kappa_{\text{h}}$ values approach 0.5305 with increasing temperature, as predicted by the high-temperature theoretical limit (Eq. 11; Matsuhisa et al., 1978; Young et al., 2002).

Unlike for $^{18}\beta_{\text{h,sc}}$ predictions, $^{17}\kappa_{\text{h,sc}}$ values calculated using PES ω scaling factors do not greatly deviate from their unscaled counterparts (Fig. S10), as observed previously (Cao and Liu, 2011). For example, $^{17}\kappa_{\text{h,sc}}$ offsets using the all-compound average scaling factors at 25 °C range from -5.9×10^{-5} [$\text{SO}_{(\text{g})}$] to -3.2×10^{-6} [$\text{H}_2\text{O}_{(\text{vap.})}$] for CCSD/aug-cc-pVTZ and from -4.0×10^{-5} [$\text{SO}_{(\text{g})}$] to -2.2×10^{-6} [$\text{H}_2\text{O}_{(\text{vap.})}$] for MP2/aug-cc-pVTZ. Offsets reach slightly larger values when using redox-state specific scaling factors, but still only range from -1.6×10^{-4} [(S) $\text{SO}_{2(\text{g})}$] to -1.2×10^{-6} [$\text{H}_2\text{O}_{(\text{vap.})}$] for CCSD/aug-cc-pVTZ and from -9.3×10^{-5} [(S) $\text{SO}_{2(\text{g})}$] to 3.6×10^{-5} [$\text{SO}_{2(\text{g})}$] for MP2/aug-cc-pVTZ.

Similarly, anharmonic ZPE correction factors lead to only small offsets between $^{17}\kappa_{\text{AnZPE}}$ and $^{17}\kappa_{\text{h}}$ (Fig. S11). For example, differences between $^{17}\kappa_{\text{AnZPE}}$ and $^{17}\kappa_{\text{h}}$ values at 25 °C using the all-compound average AnZPE correction factors range from -2.1×10^{-4} [$\text{SO}_{3(\text{g})}$] to 1.6×10^{-4} [$\text{O}_{2(\text{g})}$] for B3LYP/6-31+G(d,p) and from -1.4×10^{-4} [$\text{H}_2\text{O}_{(\text{vap.})}$] to 1.5×10^{-4} [$\text{SO}_{2(\text{g})}$] for MP2/aug-cc-pVTZ. Unlike all other variables, all-compound average and redox-state specific anharmonic ZPE correction factors yield nearly identical $^{17}\kappa_{\text{AnZPE}}$. However, anharmonic ZPE correction factors also lead to diverging predictions with increasing temperature. That is, $^{17}\kappa_{\text{AnZPE}}$ does not converge on 0.5305 as $T \rightarrow \infty$, as is theoretically predicted (Eq. 11; Matsuhisa et al., 1978; Young et al., 2002). As detailed in Cao and Liu (2011), this results from the $^{17}\text{AnZPE}/^{18}\text{AnZPE}$ term, which itself does not converge on 0.5305 as $T \rightarrow \infty$.

Based on these results, we choose to scale aqueous-phase ω values determined using the B3LYP/6-31+G(d,p) method by redox-

state specific CCSD/aug-cc-pVTZ PES scaling factors when calculating all fractionation factors. The reason for choosing CCSD/aug-cc-pVTZ rather than MP2/aug-cc-pVTZ scaling factors is twofold: (i) MP2/aug-cc-pVTZ ω and ν values for diatomic molecules are offset from experimental results (Fig. S2, S4), and (ii) MP2/aug-cc-pVTZ PES and scaling factors do not follow the expected trend with sulfur redox-state (Fig.S2–S3). Furthermore, redox-state specific scaling factors yield much closer agreement with experimental results than do all-compound average scaling factors (i.e., lower RMSE), particularly for sulfate species (Section 4.3–4.6). We do not directly employ any anharmonic ZPE corrections to aqueous-phase RPFs due to the computational limitations of directly determining \ast AnZPE for large water clusters. Rather, we qualitatively discuss potential impacts of anharmonicity in light of the observed $\leq 1\%$ $^{18}\beta_{\text{AnZPE}}$ offsets observed here for gas-phase sulfoxo species using the B3LYP/6-31+G(d,p) method. All fractionation factors reported here are thus calculated using $^{18}\beta_{\text{h,Sc}}$ and $^{17}\kappa_{\text{h,Sc}}$ scaled redox-state specific CCSD/aug-cc-pVTZ PES scaling factors.

4.2. Liquid water

Calculated $^{18}\beta_{\text{h,Sc}}$ and $^{17}\kappa_{\text{h,Sc}}$ values display some variability for individual water molecule isotope substitutions; however, cluster-average values for each water droplet are identical across all temperatures ($n = 5$; Fig. S12). Results therefore suggest minimal variability due to droplet geometry. Still, to account for effects that are not captured by the water droplet method, we additionally calculate “semi-empirical” (subscript “se”) liquid water $^{18}\beta_{\text{se}}$ and $^{17}\kappa_{\text{se}}$ values following Hayles et al. (2018). First, we combine theoretical $^{18}\beta_{\text{h,Sc}}$ values for $\text{H}_2\text{O}_{(\text{vap.})}$ calculated using the B3LYP/6-31+G(d,p) method with empirically measured $^{18}\alpha_{\text{liq./vap.}}$ from Horita et al. (2008) (their Eq. 20) to determine $^{18}\beta_{\text{se}}$ for $\text{H}_2\text{O}_{(\text{liq.})}$ using Eq. 9. We then calculate $^{17}\alpha_{\text{liq./vap.}}$ as a function of $^{18}\alpha_{\text{liq./vap.}}$ and $^{17}\theta_{\text{liq./vap.}}$ using Eq. 3. However, $^{17}\theta_{\text{liq./vap.}}$ has not yet been empirically determined with sufficient precision across the entire temperature range of interest (cf., Barkan and Luz, 2005). We therefore theoretically estimate $^{17}\theta_{\text{liq./vap.}}$ using $^{18}\beta_{\text{h,Sc}}$ and $^{17}\kappa_{\text{h,Sc}}$ values calculated with the B3LYP/6-31+G(d,p) method for $\text{H}_2\text{O}_{(\text{liq.})}$ and $\text{H}_2\text{O}_{(\text{vap.})}$ following Eq. 12. Resulting theoretical $^{17}\theta_{\text{liq./vap.}}$ agrees with available empirical results to within 2.0×10^{-4} , suggesting that our predictions are robust (Fig. S13; Barkan and Luz, 2005). We then determine $^{17}\beta_{\text{se}}$ for $\text{H}_2\text{O}_{(\text{liq.})}$ as:

$$^{17}\beta_{\text{se}} = (^{18}\alpha_{\text{liq./vap.}})^{^{17}\theta_{\text{liq./vap.}}} \times ^{17}\beta_{\text{h,Sc}}, \quad (17)$$

where $^{17}\beta_{\text{h,Sc}}$ here refers to the values for $\text{H}_2\text{O}_{(\text{vap.})}$ calculated using the B3LYP/6-31+G(d,p) method with redox-state specific CCSD/aug-cc-pVTZ scaling factors. Finally, $^{17}\kappa_{\text{se}}$ is determined following Eq. 10. To test the influence of salinity on resulting fractionations, we additionally repeat this process using empirically measured $^{18}\alpha_{\text{liq./vap.}}$ values for a 4 M NaCl solution from Horita et al. (1995) (their Eq. 10).

Resulting freshwater $^{18}\beta_{\text{se}}$ calculated here only deviates from pure theoretical predictions by a maximum of 1.7‰ and from semi-empirical values reported in Hayles et al. (2018) by a maximum of 3.8‰ (Fig. S13A). Similarly, freshwater $^{17}\kappa_{\text{se}}$ agrees with theoretical results and with semi-empirical results of Hayles et al. (2018) to within 2.5×10^{-5} , indicating that isotope effects not captured by the water droplet method are small (Fig. S13B). Furthermore, salinity exhibits a negligible effect on both $^{18}\beta_{\text{se}}$ and $^{17}\kappa_{\text{se}}$, leading to maximum deviations from freshwater results of only 0.4‰ and $< 1 \times 10^{-6}$, respectively. We therefore use freshwater $^{18}\beta_{\text{se}}$ and $^{17}\kappa_{\text{se}}$ when calculating all sulfoxoanion fractionation factors below (Section 4.3–4.6). Nonetheless, seventh-order

polynomial fits for calculating theoretical, semi-empirical (freshwater), and semi-empirical (saline) $^{18}\beta$ and $^{17}\kappa$ values as a function of temperature are reported in Tables 1,2.

4.3. Aqueous sulfate species

On average, sulfate species geometries are similar to those calculated by Eldridge et al. (2016), with bond lengths differing by a maximum of 0.01Å and angles differing by a maximum of 3.1° (Fig. 1; Table S3). Replicate $\text{SO}_3(\text{OH})^-$ geometries calculated here show nearly identical S-O bond lengths, differing by only 0.01Å. However, replicate S-(OH) and O-H bond lengths differ by up to 0.10Å and 0.09Å; similarly, O-S-O, O-S-(OH), and S-O-H bond angles differ by up to 4.0°, 4.2°, and 6.4° between replicates, likely due to the influence of H_2O geometry on hydrogen bond length and angle. Despite these geometric differences, $^{18}\beta_{\text{h,Sc}}$ and $^{17}\kappa_{\text{h,Sc}}$ are nearly identical across replicates (Fig. 2). This leads to standard deviations in $^{18}\alpha_{\text{SO}_3(\text{OH})^-/\text{H}_2\text{O}(\text{liq.})}$ and $\Delta\Delta' ^{17}\text{O}_{\text{SO}_3(\text{OH})^-/\text{H}_2\text{O}(\text{liq.})}$ of only $\pm 0.6\%$ and $\pm 0.002\%$ at 25 °C ($n = 3$; Fig. 3), which is near typical analytical precision. Seventh-order polynomial fits for calculating $^{18}\beta_{\text{h,Sc}}$ and $^{17}\kappa_{\text{h,Sc}}$ values [replicate average results for $\text{SO}_3(\text{OH})^-$] are reported in Tables 1,2.

Resulting $^{18}\alpha_{\text{SO}_4^{2-}/\text{H}_2\text{O}(\text{liq.})}$ and $^{18}\alpha_{\text{SO}_3(\text{OH})^-/\text{H}_2\text{O}(\text{liq.})}$ values are in close agreement with all previous experimental and theoretical data for dissolved sulfate and sulfate-bearing minerals (Table S5; Lloyd, 1968; Kusakabe and Robinson, 1977; Chiba et al., 1981; Zeebe, 2010; Schauble and Young, 2021). Comparing dissolved sulfate experimental results to SO_4^{2-} predictions yields an RMSE of 4.5‰, much larger than expected analytical precision. However, this RMSE decreases substantially to 1.6‰ when comparing to $\text{SO}_3(\text{OH})^-$, rather than SO_4^{2-} , predictions (Fig. 3A). As pointed out by Mizutani and Rafter (1969) and Zeebe (2010), dissolved sulfate was actually present as $\text{SO}_3(\text{OH})^-$ under the experimental conditions used in Lloyd (1968), consistent with our predictions. Anhydrite results of Chiba et al. (1981) are similarly better described by $^{18}\alpha_{\text{SO}_3(\text{OH})^-/\text{H}_2\text{O}(\text{liq.})}$ predictions than by $^{18}\alpha_{\text{SO}_4^{2-}/\text{H}_2\text{O}(\text{liq.})}$ predictions. As discussed in Chiba et al. (1981), this likely results from the smaller ionic radius of the Ca^{2+} cation in anhydrite relative to the Ba^{2+} cation used to precipitate barite for dissolved sulfate isotope analysis; smaller ionic radius and lower cation mass has been shown to lead to larger oxygen isotope fractionation (O’Neil et al., 1969). Chiba et al. (1981) therefore hypothesized that the agreement between dissolved-phase $\text{SO}_3(\text{OH})^-$ and solid-phase CaSO_4 fractionation results from similar bonding environments between these two species. This is confirmed by the barite experimental results of Kusakabe and Robinson (1977), which show smaller $^{18}\alpha_{\text{BaSO}_4/\text{H}_2\text{O}(\text{liq.})}$ relative to the $^{18}\alpha_{\text{CaSO}_4/\text{H}_2\text{O}(\text{liq.})}$ of Chiba et al. (1981) at a given temperature. Similarly, lattice-dynamic theoretical results of Schauble and Young (2021) predict that BaSO_4 equilibrium fractionation is ≈ 3 to 5‰ smaller than that of CaSO_4 across all temperatures, similar to the observed experimental offset and that seen here between $^{18}\alpha_{\text{SO}_4^{2-}/\text{H}_2\text{O}(\text{liq.})}$ and $^{18}\alpha_{\text{SO}_3(\text{OH})^-/\text{H}_2\text{O}(\text{liq.})}$ (Fig. 3A), further supporting the interpretation of Chiba et al. (1981).

Importantly, $^{18}\alpha_{\text{SO}_4^{2-}/\text{H}_2\text{O}(\text{liq.})}$ values calculated here between 0 °C and 150 °C are in close agreement with predictions from Zeebe (2010) (their Eq. 5), exhibiting an RMSE of 0.5‰ (Fig. 3A). This agreement occurs despite the conclusion by Zeebe (2010) that MP2 or B3LYP functionals yield unstable geometries and inaccurate scaling factors for hydrated SO_4^{2-} . However, the basis sets tested by Zeebe (2010) for B3LYP and MP2 functionals did not include hydrogen atom polarization functions, which are necessary to minimize basis set superposition error when using DFT methods

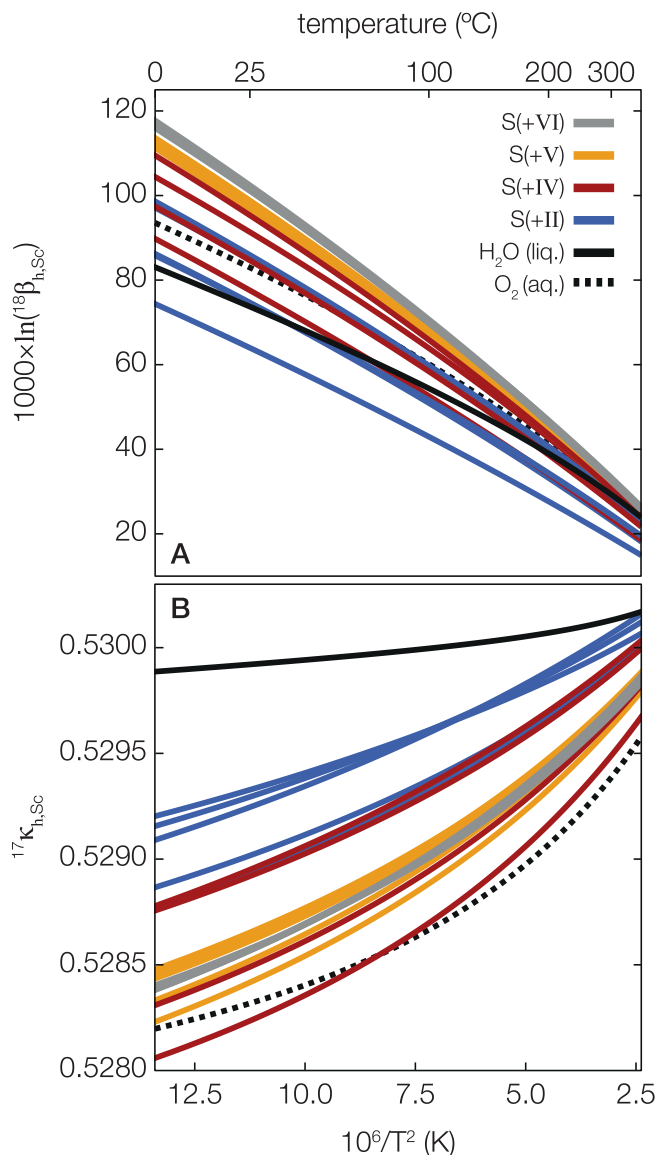


Fig. 2. Calculated $^{18}\beta_{h,Sc}$ and $^{17}\kappa_{h,Sc}$ values for all oxygen-containing solvated species. (A) $^{18}\beta_{h,Sc}$ and (B) $^{17}\kappa_{h,Sc}$ plotted as a function of temperature. Line styles refer to each species or sulfur redox state: solid black = $H_2O(liq.)$, dotted black = $O_2(aq.)$, blue = sulfoxylate species, S(+II); red = sulfite species, S(+IV); yellow = thio-sulfate species, S(+V) (sulfonate group); gray = sulfate species, S(+VI). All species within a given sulfur redox state are plotted with the same line styles.

for systems with hydrogen bonds (Novoa and Sosa, 1995). By including hydrogen atom polarization functions, our results never yielded unstable geometries (i.e., imaginary frequencies) for any sulfate species at any water droplet cluster size (Supplementary Data). Furthermore, the agreement between $^{18}\alpha$ values predicted here with past experimental and theoretical results confirms our choice of PES scaling factors. In contrast, the use of unscaled $^{18}\beta_h$ would have led to $^{18}\alpha_{SO_4^{2-}/H_2O(liq.)}$ and $^{18}\alpha_{SO_3(OH)^-/H_2O(liq.)}$ predictions that differ from experimental and previous theoretical results by up to 10‰ at Earth-surface temperatures.

Currently, no experimental $\Delta\Delta^{17}O$ data exist with which we can compare our theoretical results. Still, predicted $\Delta\Delta^{17}O_{SO_4^{2-}/H_2O(liq.)}$ and $\Delta\Delta^{17}O_{SO_3(OH)^-/H_2O(liq.)}$ values are nearly identical across all temperatures, differing by a maximum of 0.009‰ at 0 °C (Fig. 3B). Interestingly, both species yield large negative $\Delta\Delta^{17}O$ predictions (i.e., $\Delta^{17}O$ values less than that of surrounding water), reaching values as low as -0.199% at 0 °C. Predicted frac-

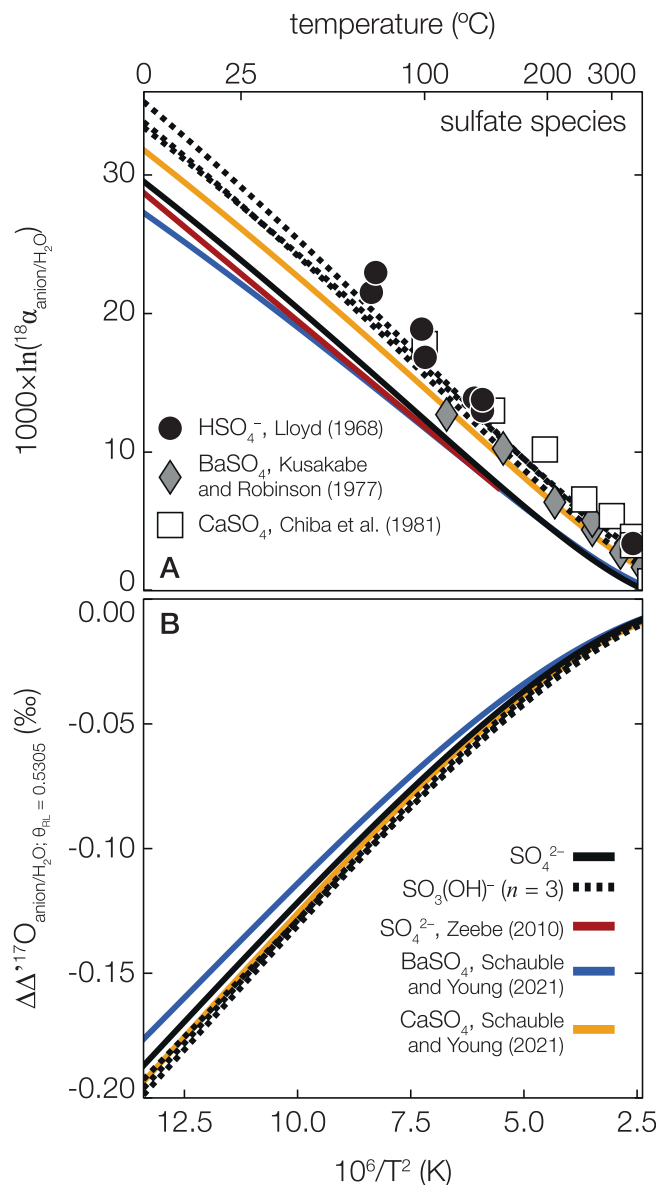


Fig. 3. Triple-oxygen equilibrium fractionation factors between liquid water and sulfate species. Predicted (A) $1000 \times \ln(^{18}\alpha)$ and (B) $\Delta\Delta^{17}O$ between each sulfate species [SO_4^{2-} ; $SO_3(OH)^-$, $n = 3$ replicates] and “semi empirical” liquid water using $^{18}\beta_{h,Sc}$ and $^{17}\kappa_{h,Sc}$ values calculated by Tables 1 and 2. Also shown in panel (A): experimental results for dissolved HSO_4^- over a range of pH conditions (Lloyd, 1968), experimental results for barite mineral ($BaSO_4$) in saline hydrothermal conditions (Kusakabe and Robinson, 1977), experimental results for anhydrite mineral ($CaSO_4$) at high-pressure hydrothermal conditions (Chiba et al., 1981), and *ab initio* predictions for SO_4^{2-} calculated using the Hartree Fock method (Zeebe, 2010). Also shown in both panels: theoretical predictions for $BaSO_4$ and $CaSO_4$ calculated using the lattice dynamics method (Schauble and Young, 2021). Panel (B) values correspond to $^{17}\theta_{RL} = 0.5305$ in the definition of $\Delta\Delta^{17}O$.

tions for both ^{18}O and ^{17}O decrease with increasing temperature, as expected. These results are again nearly identical to the solid-phase $BaSO_4$ and, especially, $CaSO_4$ predictions of Schauble and Young (2021), which were calculated using a similar theoretical method but with independent input data (i.e., lattice dynamics; Fig. 3B).

4.4. Aqueous sulfite species

Similar to sulfate, sulfite species geometries calculated here are in close agreement with those reported in Eldridge et al. (2016),

with bond lengths differing by a maximum of 0.03Å and angles differing by a maximum of 2.5° (Fig. 1; Table S3). However, unlike for sulfate species, there exist large differences in $^{18}\beta_{h,sc}$ and $^{17}\kappa_{h,sc}$ between sulfite species (Fig. 2). Across all temperatures, (HS)O₃⁻ consistently exhibits the highest $^{18}\beta_{h,sc}$ values whereas SO₃²⁻ consistently exhibits the lowest values. In contrast, SO₃²⁻ displays the highest $^{17}\kappa_{h,sc}$ values whereas SO_{2(aq)}} displays the lowest values. Seventh-order polynomial fits for calculating $^{18}\beta_{h,sc}$ and $^{17}\kappa_{h,sc}$ values for all sulfite species are reported in Tables 1,2.

These differences in $^{18}\beta_{h,sc}$ and $^{17}\kappa_{h,sc}$ lead to large differences in $^{18}\alpha$ and $\Delta\Delta'^{17}O$ predictions between different sulfite species and water (Fig. 4). For example, our results predict that (HS)O₃⁻ is 18.2‰ more enriched than SO₃²⁻ when both are in equilibrium with water at 25 °C. Similarly, estimated $\Delta\Delta'^{17}O$ for SO₃²⁻ is 0.090‰ higher than that for SO_{2(aq)}} when both are in equilibrium with H₂O at 25 °C; still, all species display $\Delta\Delta'^{17}O$ values lower than that of equilibrated water across all temperatures.

Interestingly, $^{18}\alpha_{SO_3^{2-}/H_2O(liq.)}$ and $^{18}\alpha_{SO_2(OH)^-/H_2O(liq.)}$ values calculated here drop below unity at 72 °C and 193 °C, respectively. Above these temperatures, we predict that SO₃²⁻ and SO_{2(OH)}⁻ are more depleted in ¹⁸O relative to H₂O. Similar crossovers have been observed previously for other oxygen-bearing species (e.g., Hayles et al., 2018). In contrast, all other species exhibit $^{18}\alpha$ values as high as 26.4‰ at 0 °C and do not display crossover points. Unlike for $^{18}\alpha$, $\Delta\Delta'^{17}O$ predictions never exhibit crossover points and instead trend toward zero at high temperature for all species, as expected (Young et al., 2002).

All existing experimental sulfite $^{18}\alpha$ results are in relatively close agreement with predictions calculated here (Fig. 4A, Table S5; Müller et al., 2013a; Wankel et al., 2014, this study). Experiments were performed at a range of pH values from ≈ 2 to ≈ 10, leading to large differences in isomer relative abundances between experimental conditions. We therefore compare experimental results to predicted “bulk solution” fractionation; i.e., the temperature- and pH-specific abundance-weighted average frac-

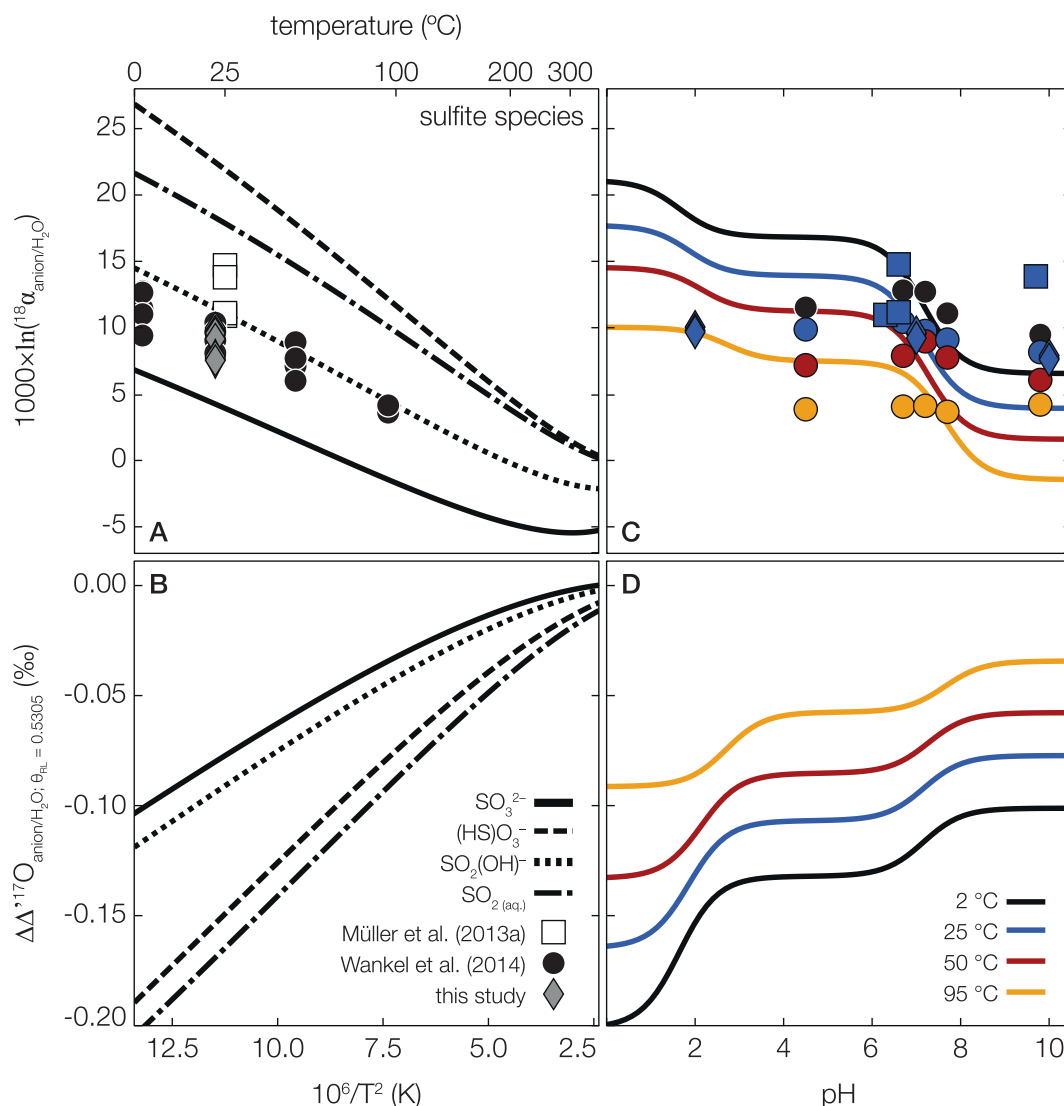


Fig. 4. Triple-oxygen fractionation factors between liquid water and sulfite species. Predicted (A) $1000 \times \ln(^{18}\alpha)$ and (B) $\Delta\Delta'^{17}O$ between each sulfite species [SO₃²⁻, (HS)O₃⁻, SO_{2(OH)}⁻, and SO_{2(aq)}}] and “semi empirical” liquid water using $^{18}\beta_{h,sc}$ and $^{17}\kappa_{h,sc}$ values calculated by Tables 1 and 2. Predicted “bulk solution” (C) $1000 \times \ln(^{18}\alpha)$ and (D) $\Delta\Delta'^{17}O$ as a function of pH for the four temperatures in which experimental data exist: 2 °C (black), 25 °C (blue), 50 °C (red), and 95 °C (yellow). Temperature- and pH-specific relative abundances of each species were calculated using the speciation constants and isomerization ratio of Millero et al. (1989) and Eldridge et al. (2018) (Fig. S14A). Also shown in panel (A) and (C): experimental results for dissolved sulfite over a range of temperature and pH conditions from three laboratories (Müller et al., 2013a; Wankel et al., 2014, this study). Experiments performed at 4 °C and 22 °C are plotted as 2 °C and 25 °C, respectively. Panel (B) and (D) values correspond to $^{17}\theta_{RL} = 0.5305$ in the definition of $\Delta\Delta'^{17}O$.

tionation factors. Speciation diagrams (Fig. S14A) were determined using the dissociation constants of Miller et al. (1989) (based on data from Goldberg and Parker, 1985) and the bisulfite isomerization ratio of Eldridge et al. (2018) assuming a dilute solution (i.e., pure water; see also Horner and Connick, 1986; Littlejohn et al., 1992; Damian et al., 2007, for further discussion on isomerization ratio estimates). This yields an overall experimental vs. predicted bulk solution RMSE of 3.7%.

Experimental vs. predicted agreement is closest at circumneutral pH when SO_3^{2-} and total bisulfite occur in roughly equal proportion, as expected given that experimental results consistently lie between SO_3^{2-} and $\text{SO}_2(\text{OH})^-$ predictions (Fig. 4A). In contrast, bulk solution theoretical results over-predict low-pH experiment $^{18}\alpha$ values by as much as 6‰ and under-predict high-pH experiment $^{18}\alpha$ values by as much as 10‰ (Fig. 4C; Fig. S14B) due to the fact that experimental results are relatively insensitive to pH. For example, this can be seen by comparing all experimental results to predicted $^{18}\alpha_{\text{SO}_2(\text{OH})^-/\text{H}_2\text{O}(\text{liq.})}$ values; this yields an RMSE of 2.2‰, much lower than for the bulk solution, despite the fact that $\text{SO}_2(\text{OH})^-$ alone never dominates the bulk sulfite solution. As discussed at length in Müller et al. (2013a), retaining accurate isotope signatures during experimental conversion to SO_3^{2-} and subsequent precipitation as BaSO_3 is challenging due to (i) potential kinetic fractionation effects (ii), incorporation of H_2O molecules into the hygroscopic salt, and (iii) potential biases toward a particular species or isomer [e.g., $\text{SO}_2(\text{OH})^-$] during the precipitation reaction. It therefore remains unclear if theory vs. experiment offsets are largely due to (i) inadequacies in the theoretical predictions, (ii) the influence of unknown (non-equilibrium) experimental isotope effects, or (iii) some combination of these factors. This discrepancy may be reconciled in the future by measuring oxygen-isotope compositions of intact aqueous sulfoxyanions using high-resolution mass spectrometry techniques (e.g., Neubauer et al., 2020).

4.5. Aqueous sulfoxylate species

Sulfoxylate species geometries again agree closely with those calculated in Eldridge et al. (2016); bond lengths differ by a maximum of 0.02Å and geometries differ by a maximum of 2.7° (Fig. 1; Table S3). Like for sulfite species, there exist large differences in $^{18}\beta_{\text{h,sc}}$ and $^{17}\kappa_{\text{h,sc}}$ between sulfoxylate species (Fig. 2). For example, we predict that $^{18}\alpha_{(\text{HS})\text{O}(\text{OH})/\text{H}_2\text{O}(\text{liq.})}$ is 22.5‰ higher than $^{18}\alpha_{\text{SO}_2^{2-}/\text{H}_2\text{O}(\text{liq.})}$ at 25 °C (Fig. 5A). Similarly, predicted $\Delta^{17}\text{O}$ for SO_2^{2-} in equilibrium with H_2O at 25 °C is 0.049‰ higher than that predicted for $(\text{HS})\text{O}(\text{OH})$ at the same temperature (Fig. 5B).

Interestingly, $^{18}\alpha$ results for all sulfoxylate species either yield a crossover point [for $(\text{HS})\text{O}_2^-$, $\text{SO}(\text{OH})^-$, $(\text{HS})\text{O}(\text{OH})$, and $\text{S}(\text{OH})_2$] or predict ^{18}O depletion relative to H_2O across the entire temperature range considered [for SO_2^{2-}]. Unlike for sulfoxyanion species at all other redox states, this additionally leads to crossovers in $\Delta^{17}\text{O}$; specifically, SO_2^{2-} reaches $\Delta^{17}\text{O}$ values that are 0.003‰ higher than that of equilibrated water at 350 °C. Because little is known about the role of sulfoxylate species in the global sulfur cycle, there exist no experimental isotope fractionation results with which we can compare our predictions. Nonetheless, seventh-order polynomial fits for calculating $^{18}\beta_{\text{h,sc}}$ and $^{17}\kappa_{\text{h,sc}}$ values for all sulfoxylate species are reported in Tables 1, 2.

4.6. Aqueous thiosulfate species

Finally, $\text{S}_2\text{O}_3^{2-}$ also displays a similar geometry to that calculated in Eldridge et al. (2016) (all other thiosulfate species were not

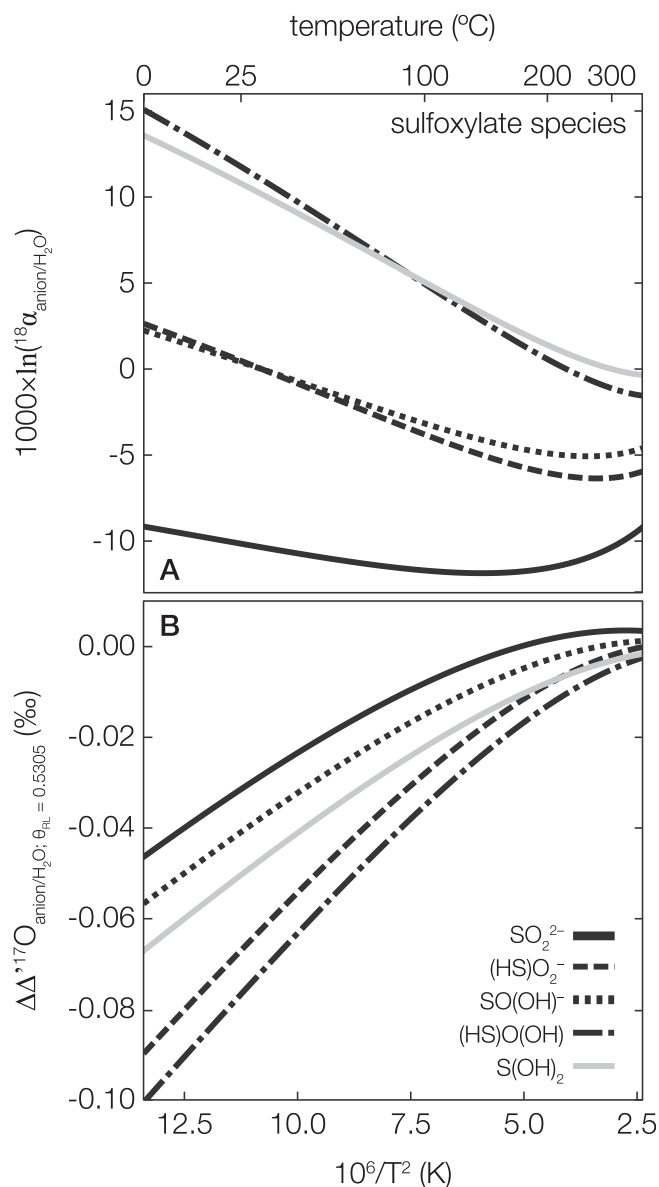


Fig. 5. Triple-oxygen fractionation factors between liquid water and sulfoxylate species. Predicted (A) $1000 \times \ln(^{18}\alpha)$ and (B) $\Delta\Delta^{17}\text{O}$ between each sulfoxylate species [SO_2^{2-} , $(\text{HS})\text{O}_2^-$, $\text{SO}(\text{OH})^-$, $(\text{HS})\text{O}(\text{OH})$, and $\text{S}(\text{OH})_2$] and “semi empirical” liquid water using $^{18}\beta_{\text{h,sc}}$ and $^{17}\kappa_{\text{h,sc}}$ values calculated by Tables 1 and 2. Panel (B) values correspond to $^{17}\theta_{\text{RL}} = 0.5305$ in the definition of $\Delta^{17}\text{O}$.

included in their study); bond lengths differ by a maximum of 0.01Å and geometries differ by a maximum of 0.4° (Fig. 1; Table S3). Like $\text{SO}_3(\text{OH})^-$, we additionally calculated triplicate $\text{S}_2\text{O}_2(\text{OH})^-$ geometries and fractionation factors. Replicate geometries show similar bond lengths, with differences reaching 0.02Å for S-O bonds, 0.03Å for S-S and S-(OH) bonds, and 0.04Å for O-H bonds. Bond angle differences between replicates reach 2.2° for O-S-O, 3.2° for S-O-H, 3.6° for S-S-(OH), 3.8° for S-S-O, and 5.2° for O-S-(OH). Despite these geometric differences, $^{18}\beta_{\text{h,sc}}$ and $^{17}\kappa_{\text{h,sc}}$ are again nearly identical across replicates (Fig. 2), leading to standard deviations in $^{18}\alpha_{\text{S}_2\text{O}_2(\text{OH})^-/\text{H}_2\text{O}(\text{liq.})}$ and $\Delta\Delta^{17}\text{O}_{\text{S}_2\text{O}_2(\text{OH})^-/\text{H}_2\text{O}(\text{liq.})}$ of only $\pm 0.2\text{‰}$ and $\pm 0.001\text{‰}$ at 25 °C ($n = 3$; Fig. 6), well within analytical precision.

Resulting $^{18}\alpha_{\text{S}_2\text{O}_3^{2-}/\text{H}_2\text{O}(\text{liq.})}$ and $^{18}\alpha_{\text{S}_2\text{O}_2(\text{OH})^-/\text{H}_2\text{O}(\text{liq.})}$ predictions behave similarly to their sulfate-species counterparts; furthermore, $^{18}\alpha_{(\text{HS})\text{SO}_3^-/\text{H}_2\text{O}(\text{liq.})}$ is nearly identical to $^{18}\alpha_{\text{S}_2\text{O}_2(\text{OH})^-/\text{H}_2\text{O}(\text{liq.})}$

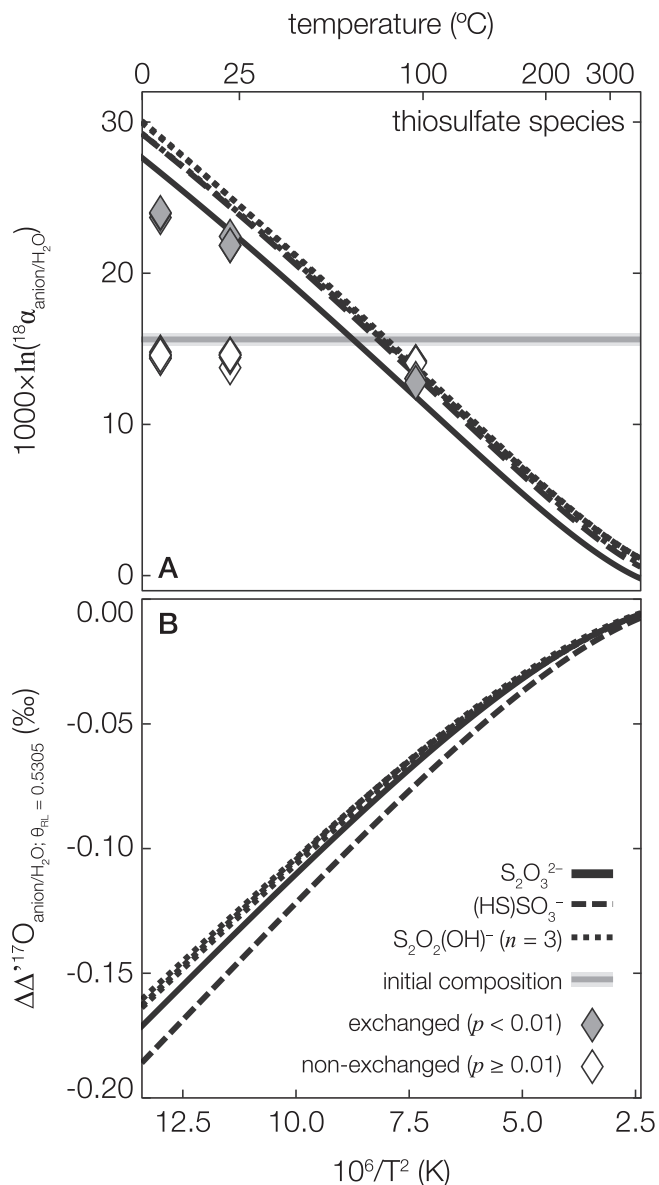


Fig. 6. Triple-oxygen fractionation factors between liquid water and thiosulfate species. Predicted (A) $1000 \times \ln(\alpha)$ and (B) $\Delta\Delta'^{17}\text{O}$ between each thiosulfate species [$\text{S}_2\text{O}_3^{2-}$; $(\text{HS})\text{SO}_3^-$; and $\text{S}_2\text{O}_2(\text{OH})^-$, $n = 3$ replicates] and “semi empirical” liquid water using $^{18}\beta_{\text{h,sc}}$ and $^{17}\kappa_{\text{h,sc}}$ values calculated by Tables 1 and 2. Panel (B) values correspond to $^{17}\theta_{\text{RL}} = 0.5305$ in the definition of $\Delta'^{17}\text{O}$. Also shown in panel (A): experimental results for dissolved thiosulfate over a range of temperature and pH conditions (this study). White diamonds indicate experiments whose ^{18}O composition was statistically identical before and after experimental treatment, implying no oxygen-isotope exchange. Gray diamonds indicate experiments whose final ^{18}O composition was statistically different from the starting composition, indicating isotope exchange.

across all temperatures (Fig. 6A). For example at 25 °C, we predict $^{18}\alpha_{\text{S}_2\text{O}_3^{2-}/\text{H}_2\text{O}(\text{liq})}$ and $^{18}\alpha_{\text{S}_2\text{O}_2(\text{OH})^-/\text{H}_2\text{O}(\text{liq})}$ values of 24.1‰ and 26.3‰, compared to 24.8‰ and 28.6‰ for $^{18}\alpha_{\text{SO}_4^{2-}/\text{H}_2\text{O}(\text{liq})}$ and $^{18}\alpha_{\text{SO}_3(\text{OH})^-/\text{H}_2\text{O}(\text{liq})}$. This similarity between thiosulfate- and sulfate-species fractionations additionally extends to $\Delta\Delta'^{17}\text{O}$ predictions (Fig. 6B). For example at 25 °C, we estimate $\Delta\Delta'^{17}\text{O}_{\text{S}_2\text{O}_3^{2-}/\text{H}_2\text{O}(\text{liq})}$ and $\Delta\Delta'^{17}\text{O}_{\text{S}_2\text{O}_2(\text{OH})^-/\text{H}_2\text{O}(\text{liq})}$ values of -0.158‰ and -0.150‰ , whereas predicted $\Delta\Delta'^{17}\text{O}_{\text{SO}_4^{2-}/\text{H}_2\text{O}(\text{liq})}$ and $\Delta\Delta'^{17}\text{O}_{\text{SO}_3(\text{OH})^-/\text{H}_2\text{O}(\text{liq})}$ values are -0.154‰ and -0.161‰ . Overall, this close agreement between isotope fractionation for sulfate and thiosulfate species

likely results from the fact that oxygen exchange occurs at the S (+V) sulfonate atom—rather than the S(-I) sulfonyl atom (Pryor and Tonellato, 1967)—which is described by a similar bonding environment and ZPE to that of the sulfate sulfur atom.

Few reliable experimental equilibrium exchange fractionation factor estimates exist for thiosulfate species. We compare our predictions to experimental results also presented in this study; however, it is likely that oxygen isotope equilibrium was not reached under some experimental conditions. We therefore exclude from our comparison any experimental results that are statistically identical to the $\text{Na}_2\text{S}_2\text{O}_3$ starting material $\delta^{18}\text{O}$ value ($p < 0.01$; two-tailed t test; Table S5). This leads to an RMSE between our predictions and retained experimental data of 2.2‰ when comparing to $^{18}\alpha_{\text{S}_2\text{O}_3^{2-}/\text{H}_2\text{O}(\text{liq})}$, 3.2‰ when comparing to $^{18}\alpha_{(\text{HS})\text{SO}_3^-/\text{H}_2\text{O}(\text{liq})}$, and 3.6‰ when comparing to $^{18}\alpha_{\text{S}_2\text{O}_2(\text{OH})^-/\text{H}_2\text{O}(\text{liq})}$. Interestingly, unlike for sulfate and sulfite species, thiosulfate RMSE is highest when comparing to the $\text{S}_2\text{O}_2(\text{OH})^-$ isomer, although the exact proportion of protonated thiosulfate at our experimental conditions remains unknown. However, this RMSE should be considered a maximum estimate since it remains possible that isotope exchange remained incomplete in these experiments. Like all other sulfoxyanion species, no experimental $\Delta\Delta'^{17}\text{O}$ data exist with which we can compare our theoretical results.

5. Discussion and implications

We discuss how these equilibrium fractionation factors update our understanding of several sulfur-cycle processes—including pyrite oxidation, MSR, thiosulfate disproportionation, and hydrothermal anhydrite precipitation—that represent the major sulfur fluxes on Earth’s surface. For each process, we assess whether equilibrium predictions support or refute a certain mechanistic pathway. We focus specifically on the possible incorporation of atmospheric O_2 into sulfate, as this has been previously invoked to explain fluvial, lacustrine, and marine sulfate $\Delta'^{17}\text{O}$ values (e.g., Bao et al., 2008; Crockford et al., 2018; Killingsworth et al., 2018; Crockford et al., 2019).

5.1. Pyrite oxidation

Sulfate dissolved in modern rivers and preserved in ancient mineral deposits often displays negative $\Delta'^{17}\text{O}$ values (see Crockford et al., 2019, for compilation). This result is canonically interpreted to reflect incorporation of oxygen sourced from a mixture of water and dissolved O_2 —which carries a negative mass-independent ^{17}O signal (Thiemens and Lin, 2021)—into sulfate during pyrite oxidation (Fig. 7A; e.g., Bao et al., 2008; Crockford et al., 2018; Killingsworth et al., 2018). However, dissolved sulfate in modern rivers draining pyrite-rich lithologies has recently been shown to exhibit $\Delta'^{17}\text{O}$ values equal to or slightly higher than those of concomitant water, questioning this mechanistic interpretation (Hemingway et al., 2020).

While several aspects of the pyrite oxidation mechanism remain unknown or underconstrained (e.g., Schoonen et al., 2010), it is generally accepted that pyrite sulfur is oxidized via a multi-step electron transfer process (the so-called “semi-conductor” model; Williamson and Rimstidt, 1994). Accordingly, pyrite sulfur acts as an anode that iteratively donates electrons to cathodic iron atoms. Electropositive sulfur is subsequently subject to nucleophilic attack by H_2O or OH^- , forming sulfoxy species and releasing H^+ to solution. Direct O_2 incorporation into sulfate is thus inconsistent with the semi-conductor model, although the importance of alternative, isotopically unique nucleophiles such as H_2O_2 remains unknown (Schoonen et al., 2010; Hemingway et al., 2020).

Here, we instead hypothesize that dissolved sulfate $\delta^{18}\text{O}$ and $\Delta^{17}\text{O}$ values can reflect intermediate sulfoxyanion oxygen-isotope equilibrium with water and subsequent (possibly microbially mediated) dissolved-phase oxidation, either during initial pyrite oxidation or downstream redox cycling. We test this hypothesis using recently reported triple-oxygen isotope values

for a time-series of Mississippi River sulfate collected at Baton Rouge, Louisiana, USA (Killingsworth et al., 2018). Pyrite oxidation-derived sulfur is released to solution either as sulfite, thiosulfate, or sulfate depending on pH (e.g., Rimstidt and Vaughan, 2003). Furthermore, pyrite surfaces have been shown to catalyze thiosulfate oxidation to sulfite (Xu and Schoonen, 1995), which exhibits rapid oxygen-isotope exchange under circumneutral to acidic pH values (Betts and Voss, 1970; Wankel et al., 2014). If we assume the final oxygen atom is derived from water with a negligible kinetic isotope effect (cf., Müller et al., 2013b; Cao and Bao, 2021), then Mississippi River sulfate isotope compositions can be explained by sulfite-water equilibrium isotope exchange at pH 7 followed by terminal oxidation to sulfate (Fig. 7B). In contrast, these data are not consistent with a terminal oxygen atom derived from dissolved O_2 nor with thiosulfate isotope equilibrium followed by disproportionation (Fig. 7B), implicating sulfite as the critical intermediate sulfoxyanion.

Interestingly, this result is strongly dependent on solution pH. For example, low-pH equilibrium expected to occur in acid-mine drainage settings would exhibit much lower $\Delta^{17}\text{O}$ near -0.175‰ at 25 °C (Fig. 4D). In contrast, alkaline solutions such as those expected during carbonate- or silicate-buffered rock weathering would display smaller $\Delta^{17}\text{O}$ offsets from water at the same temperature. Thus, in addition to temperature, weathering-solution pH likely exhibits a strong control on resulting dissolved sulfate oxygen-isotope compositions.

Still, large uncertainties persist. For example, both Rimstidt and Vaughan (2003) and Kohl and Bao (2011) showed that the majority of released S can occur as thiosulfate in circumneutral to alkaline aerobic and anaerobic pyrite oxidation experiments, even after several weeks. Similarly, Hemingway et al. (2020) showed that pyrite oxidation-derived sulfate can retain anomalously positive $\Delta^{17}\text{O}$ values—possibly sourced from atmospheric H_2O_2 —although this signal is overprinted by downstream processes (e.g., biogeochemical sulfate recycling). While the mechanism of H_2O_2 signal

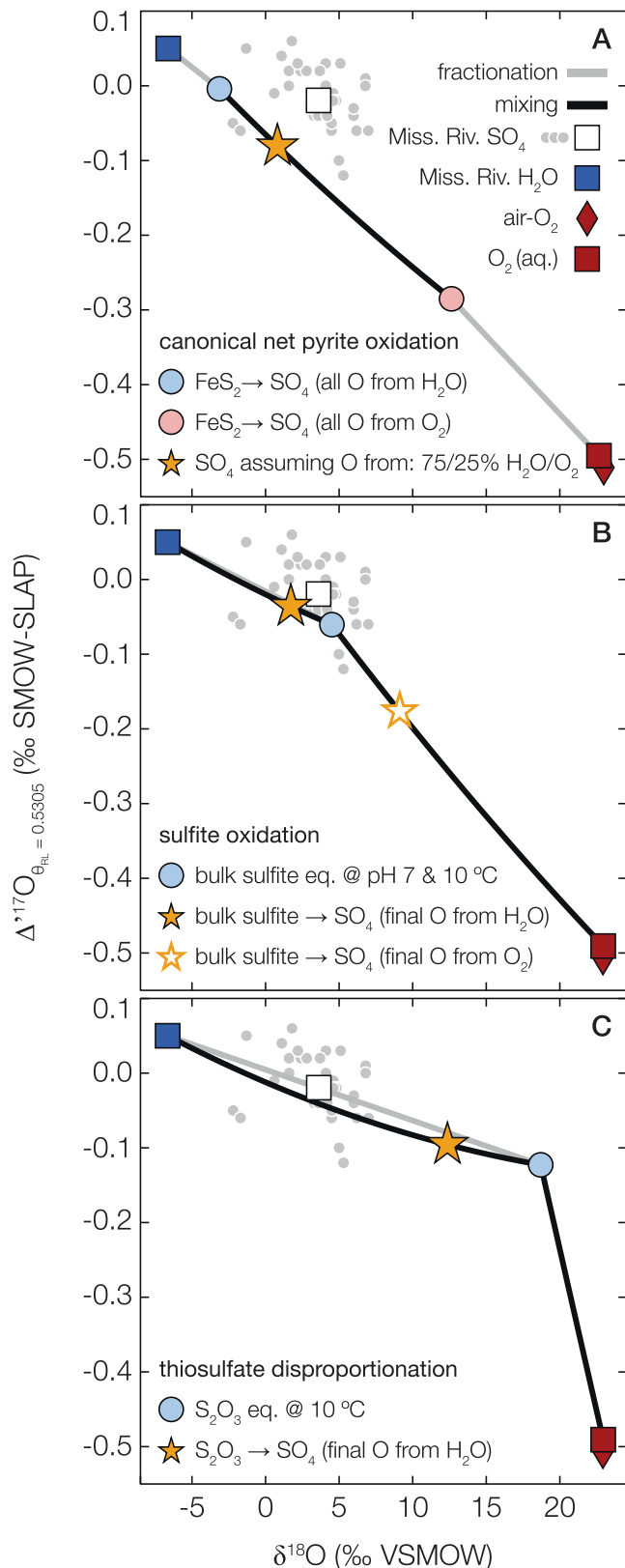


Fig. 7. New and canonical interpretations of sulfate isotope compositions in the oxidative sulfur cycle. Predicted sulfate triple-oxygen isotope compositions following: (A) canonical interpretations of experimentally observed net pyrite oxidation isotope effects, (B) sulfite-water isotope equilibrium at 10 °C and pH 7 followed by oxidation to sulfate, (C) thiosulfate-water isotope equilibrium at 10 °C followed by disproportionation to sulfate and hydrogen sulfide (Eq. 19). Mississippi River dissolved sulfate isotope compositions are used as an example dataset to test these predictions. Markers common to all panels are as follows: blue squares = average Mississippi River water at Arkansas City, AR, USA (1984–1987; $n = 10$; Coplen and Kendall, 2000; Killingsworth et al., 2018); red diamonds = atmospheric O_2 (Sharp and Wostbrock, 2021); red squares = dissolved oxygen in equilibrium with atmospheric O_2 at 10 °C (Benson and Krause, 1984; Luz and Barkan, 2009); gray circles = individual Mississippi River dissolved sulfate samples (2009–2014, $n = 38$; Killingsworth et al., 2018); white squares = Mississippi River dissolved sulfate average composition; gray lines = fractionation trajectories; black lines = mixing trajectories. Originally reported Mississippi River sulfate $\Delta^{17}\text{O}$ values have been shifted up by 0.07‰ as recommended by Cao and Bao (2021) to place results closer to the SMOW-SLAP calibration scale. For panel (A), ^{18}O values of net pyrite oxidation with all O from either H_2O or O_2 are taken from Balci et al. (2007); corresponding $\Delta\Delta^{17}\text{O}$ values have not been measured and are assumed here to follow kinetic fractionation lines with slopes defined by the reduced masses of reactants (cf., Cao and Bao, 2021, their Table 1). We assume final sulfate contains 75% O from H_2O and 25% O from O_2 , consistent with previous interpretations (Balci et al., 2007; Kohl and Bao, 2011). For panel (B), we assume T- and pH-specific bulk solution fractionation factors (see main text) and for panel (C) we assume fractionation with $\text{S}_2\text{O}_3^{2-}$. We additionally assume that sulfite/thiosulfate is quantitatively oxidized/disproportionated such that any kinetic fractionation is not expressed; fractionation of H_2O during oxidation/disproportionation is not constrained but is thought to be of minor importance (cf., Müller et al., 2013b). All $\Delta^{17}\text{O}$ values correspond to $^{17}\theta_{\text{rel}} = 0.5305$ and are reported on the SMOW-SLAP calibration scale whenever possible (Sharp and Wostbrock, 2021). Importantly, only sulfite equilibrium followed by oxidation with terminal oxygen from H_2O can explain observed Mississippi River results.

incorporation into sulfate remains unknown, Fe(II)-mediated H₂O₂ degradation has recently been shown to follow a mass law of 0.5347 ± 0.0006 (Sutherland et al., 2022); this is larger than $^{17}\theta_{\text{RL}}$ and thus leads to ^{17}O enrichment in degradation products relative to reactant H₂O₂. It is thus possible that the incorporation of Fe(II)-mediated H₂O₂ degradation products into sulfate could also explain observed positive $\Delta^{17}\text{O}$ values. In contrast, Cao and Bao (2021) reinterpreted positive $\Delta^{17}\text{O}$ values in riverine sulfate as reflecting kinetic isotope fractionation rather than H₂O₂ incorporation, although this interpretation relies on knowledge of kinetic triple-oxygen isotope fractionation factors, which remain unconstrained. Finally, the mechanism proposed here cannot explain $\Delta^{17}\text{O}$ values as low as -1.0‰ observed in Neoproterozoic sulfate deposits (Bao et al., 2008). Future laboratory- and field-based work is therefore crucial to constrain *in situ* environmental parameters such as pH, thiosulfate and sulfite concentrations and isotope compositions, and H₂O₂ concentrations at the site of pyrite oxidation.

5.2. Microbial sulfate reduction

Whereas pyrite oxidation is the dominant source of sulfate to Earth's surface, MSR and subsequent pyrite formation in marine sediments represents the dominant sink. For the purpose of tracing oxygen isotopes, MSR can be interpreted as following the simplified intracellular reaction network:



where APS refers to the adenosine phosphosulfate enzyme complex; we exclude terminal reduction of SO_3^{2-} to H₂S since this does not involve oxygen exchange (Zeebe, 2010; Wankel et al., 2014; Wing and Halevy, 2014; Bertran et al., 2020). Furthermore, the oxidative back-reaction from APS to SO_4^{2-} can occur either enzymatically or abiotically (Bertran et al., 2020; Benkovic and Hevey, 1970). In the enzymatic case, sulfate is released via nucleophilic attack on the APS phosphorus atom; one of four oxygen atoms in resulting sulfate is thus derived from the phosphate group of adenosine monophosphate (AMP; Brunner et al., 2012). In the abiotic case however, sulfate is nearly quantitatively released by a unimolecular elimination reaction, leading to sulfate with three oxygen atoms derived from sulfite and one oxygen atom directly sourced from water (Benkovic and Hevey, 1970). At Earth-surface conditions, neither sulfate nor APS are known to exchange oxygen atoms with ambient water (Chiba and Sakai, 1985; Kohl et al., 2012), implicating sulfite and AMP phosphate as the primary species by which oxygen-isotope exchange can occur.

Depending on thermodynamic conditions and substrate concentrations—and thus sulfate reduction rates—MSR will exist between purely kinetic (i.e., unidirectional forward fluxes in Eq. 18) and equilibrium (i.e., equal forward and backward fluxes in Eq. 18) limits (Wing and Halevy, 2014). At the kinetic limit, all generated SO_3^{2-} is completely reduced to H₂S within the cell; at the equilibrium limit however, isotopically equilibrated SO_3^{2-} can back-react to SO_4^{2-} . The exact position between these limits therefore determines the degree to which equilibrium isotope exchange during MSR (including AMP phosphate-derived oxygen for the enzymatic oxidation reaction) impacts marine sulfate oxygen isotope compositions (Bertran et al., 2020). Using a thermodynamic model, Wing and Halevy (2014) estimated that MSR in marine sediments likely approaches the equilibrium limit, even in coastal regions with high sulfate reduction rates. This has since been confirmed in several field localities by tracking porewater sulfate ^{33}S and ^{34}S evolution with sediment depth; results are inconsistent with MSR operating in the kinetic regime (Masterson et al., 2018; Masterson et al., 2022). Several aspects of equilibrium oxygen iso-

tope exchange during MSR remain unknown or underconstrained, particularly regarding the timescale of AMP phosphate oxygen exchange (Brunner et al., 2012; Chang and Blake, 2015). Nevertheless, here we use our theoretical predictions to estimate two end-member scenarios that may prove useful for interpreting field results:

(i) Full expression of the sulfate-water equilibrium fractionation factor. At the equilibrium limit, Bertran et al. (2020) estimated that the abiotic elimination pathway likely dominates the oxidative APS back-reaction. If true, this implies that SO_4^{2-} (at circumneutral pH) regeneration involves an activated transition state resembling $\text{AMP} \cdots \text{SO}_3 \cdots \text{H}_2\text{O}$, which may rapidly exchange oxygen atoms with water (Benkovic and Hevey, 1970). Such a direct sulfate-water exchange mechanism has been invoked previously to explain the similarity between observed and theoretical sulfate $\delta^{18}\text{O}$ predictions (Zeebe, 2010); however, this similarity may be fortuitous rather than mechanistic (Brunner et al., 2012). Nevertheless, our results predict direct sulfate-water equilibrium during MSR would push sulfate to higher $\delta^{18}\text{O}$ and lower $\Delta^{17}\text{O}$ with a $^{17}\theta_{\text{SO}_4^{2-}/\text{H}_2\text{O}}$ value ranging from 0.5240 to 0.5243 between 0 and 25 °C. For the modern ocean, this equates to an equilibrium MSR sulfate composition with $\delta^{18}\text{O}$ ranging from 29.1 to 24.8‰ and $\Delta^{17}\text{O}$ ranging from -0.187 to -0.154‰ between 0 and 25 °C.

(ii) A weighted-average of the sulfite-water (75%) and AMP phosphate-water (25%) equilibrium fractionation factors. If we assume that the residence times of sulfite and AMP phosphate are long enough such that both reach isotopic equilibrium with water, the overall expressed sulfate-water fractionation should represent a weighted average of these two species (Brunner et al., 2012). Here, we ignore any additional fractionation between SO_3^{2-} and APS and between APS and SO_4^{2-} since their triple-oxygen fractionation factors remain unknown, although these steps may prove important. Unfortunately, AMP phosphate triple-oxygen isotope fractionation factors have also not been measured or theoretically predicted. We instead use theoretical fluoroapatite predictions from Schauble and Young (2021); these are in close agreement with experimentally derived dissolved phosphate ^{18}O fractionations and should thus serve as a useful first approximation (Chang and Blake, 2015). Assuming bulk-solution sulfite fractionation at pH 7 (Fig. S14A; Millero et al., 1989; Eldridge et al., 2018), this results in an expressed $^{17}\theta$ ranging from 0.5176 to 0.5194 for temperatures between 0 and 25 °C. For the modern ocean, this leads to equilibrium MSR-derived sulfate $\delta^{18}\text{O}$ ranging from 12.8‰ to 9.8‰ and $\Delta^{17}\text{O}$ ranging from -0.122‰ to -0.095‰ . However, these $\delta^{18}\text{O}$ values are up to 15‰ lower than porewater observations, suggesting additional fractionation during reoxidation back-reactions (Zeebe, 2010; Brunner et al., 2012).

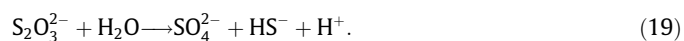
Waldeck et al. (2019) recently reported that marine sulfate is described by $\delta^{18}\text{O}$ and $\Delta^{17}\text{O}$ values of $8.67 \pm 0.21\text{‰}$ and $-0.016 \pm 0.017\text{‰}$, respectively. For both scenarios described here, this is consistent with a mixture between MSR recycling and an ^{18}O -depleted, ^{17}O -enriched input, presumably dissolved riverine sulfate (Hemingway et al., 2020). To estimate the relative importance of MSR and riverine inputs in setting observed marine signals, Waldeck et al. (2019) hypothesized a $\delta^{18}\text{O}$ value for the MSR end member ranging from 24‰ to 27‰, within our “full sulfate expression” scenario range. However, that study also assumed an MSR $^{17}\theta$ value between 0.527 and 0.5305, substantially higher than the range estimated here for both scenarios (i.e., total range of 0.5176 to 0.5243). The $^{17}\theta$ values of Waldeck et al. (2019) would lead to a less negative MSR $\Delta^{17}\text{O}$ prediction and thus—all else being equal—a greater contribution of this end member to observed marine signals relative to that predicted using the fractionation factors proposed here. Still, several aspects of the con-

trols on marine sulfate $\Delta^{17}\text{O}$ values remain unknown, particularly globally integrated riverine input values. Future studies are therefore needed to further constrain these signals.

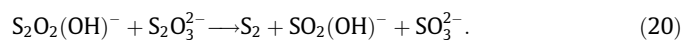
Although several aspects of MSR triple-oxygen isotope fractionation remain under-constrained, one common feature of all predictions derived here is the generation of sulfate with $\Delta^{17}\text{O}$ values lower than those of ambient water. It thus becomes clear that observed slightly negative $\Delta^{17}\text{O}$ values of fluvial and marine sulfate (Killingsworth et al., 2018; Waldeck et al., 2019) can be explained purely by sulfate-water equilibrium during MSR operating near the equilibrium limit without the need to invoke incorporation of anomalously ^{17}O -depleted dissolved O_2 .

5.3. Thiosulfate disproportionation

Thiosulfate is produced by the partial oxidation of sulfide at redox boundaries, for example when aerated water penetrates into anoxic hot springs (Xu et al., 1998) or marine sediments (Jørgensen, 1990). At circumneutral pH, bulk thiosulfate isotopically exchanges oxygen with surrounding water with a half life on the order of hours (the presence of $\text{SO}_2(\text{OH})^-$ can also act as a minor catalyst for this exchange; Pryor and Tonellato, 1967). Thiosulfate can then disproportionate either biologically or abiotically, but these two mechanisms follow unique reaction pathways. Microbial thiosulfate disproportionation has been shown to proceed as (Jørgensen, 1990; Finster et al., 1998):



In contrast, abiotic disproportionation is thought to involve a suite of reactions with the rate-limiting step described by the bimolecular reaction (Johnston and McAmish, 1973; Xu and Schoonen, 1995; Xu et al., 1998):



Assuming (i) reactant $\text{S}_2\text{O}_3^{2-}$ reaches isotopic equilibrium with water, (ii) microbial disproportionation proceeds unidirectionally (i.e., no back-reaction in Eq. 19), and (iii) the final oxygen atom is derived from water with a negligible kinetic isotope effect (cf., Cao and Bao, 2021), then microbial disproportionation will yield product sulfate with $\delta^{18}\text{O}$ and $\Delta^{17}\text{O}$ values $\approx 20\%$ higher and $\approx 0.15\%$ lower than surrounding water, respectively (Fig. 7C). While each of these assumptions must be thoroughly validated (e.g., the residence time of thiosulfate in a given environment may be too short to reach isotopic equilibrium), this calculation nevertheless provides a useful end-member scenario to interpret environmental data.

In contrast, abiotic thiosulfate disproportionation produces sulfite, which will itself rapidly exchange oxygen isotopes with surrounding water (Fig. 7B). The original thiosulfate isotope signature is therefore overprinted by sulfite oxygen exchange, independent of the degree to which reactant thiosulfate and water reached isotope equilibrium. Subsequent oxidation will yield sulfate with an isotope signature that reflects a mixing between equilibrated sulfite and the final oxygen atom source (in addition to any kinetic effects; Cao and Bao, 2021). Still, the importance of pH and temperature on thiosulfate oxygen-isotope equilibrium warrants further experimental study (cf., Eldridge et al., 2021, for related sulfur-isotope discussion).

5.4. Hydrothermal oxygen isotope exchange

Finally, we briefly consider hydrothermal oxygen-isotope exchange between water and sulfate. Although exchange is negligible at Earth-surface conditions—even over billion-year timescales—exchange rates increase drastically at elevated

temperatures characteristic of hydrothermal vents (Chiba and Sakai, 1985). Measured $\delta^{18}\text{O}$ values of laboratory hydrothermally precipitated anhydrite (CaSO_4) are consistent with our $\text{SO}_3(\text{OH})^-$ fractionation predictions (Fig. 3A; see Sec. 4.3 and Chiba et al., 1981; O'Neil et al., 1969, for discussion on the comparison between $\text{SO}_3(\text{OH})^-$ and CaSO_4 fractionation factors), supporting equilibrium exchange under these conditions, as has been suggested previously (Lloyd, 1968; Chiba et al., 1981; Zeebe, 2010). However, no hydrothermal anhydrite $\Delta^{17}\text{O}$ records currently exist to our knowledge. Nevertheless, anhydrite $\delta^{18}\text{O}$ has been used as a proxy for alteration fluid temperature at the time of mineral precipitation, although this requires that alteration fluid oxygen-isotope composition is accurately known (e.g., Teagle et al., 1998) and that anhydrite-water equilibrium is reached in natural vent settings (cf., Chiba et al., 1998). Still, if the temperature of isotope exchange can be constrained independently (e.g., by traditional or “clumped” isotope thermometry of co-existing carbonates; Weinzierl et al., 2018) and equilibrium exchange can be ensured (e.g., by additionally measuring $\delta^{34}\text{S}$; Chiba et al., 1998), then hydrothermal anhydrite veins preserved in oceanic crust and obducted ophiolites may record the triple-oxygen isotope composition of alteration fluid in the geologic past. This hypothesis remains speculative but warrants further study.

6. Conclusions

The triple-oxygen isotope composition of sulfate ($\delta^{18}\text{O}$ and $\Delta^{17}\text{O}$)—both in modern aquatic systems and in geologically preserved sulfate-bearing minerals—is becoming a common tool to constrain sulfur-cycle processes. However, equilibrium oxygen-isotope fractionation factors between water and intermediate sulfoxyanion species remain largely unknown. Here, we estimate fractionation factors for a suite of sulfoxyanions—including several protonated species—using a quantum-chemistry computational approach; our results are in relatively good agreement with all available experimental constraints, and we discuss possible experimental and theoretical means of improving agreement, especially for the sulfite system. We highlight the potential importance of short-lived thiosulfate and, especially, sulfite species in setting $\delta^{18}\text{O}$ and $\Delta^{17}\text{O}$ values of sulfate produced by several abiotic and biological processes (e.g., pyrite oxidation, MSR, thiosulfate disproportionation, anhydrite precipitation). Importantly, when equilibrium sulfite or thiosulfate fractionation factors are expressed, resulting sulfate can exhibit $\Delta^{17}\text{O}$ values up to $\approx 0.20\%$ lower than equilibrated water. Slightly negative $\Delta^{17}\text{O}$ values thus do not require incorporation of alternative oxygen sources such as dissolved O_2 , as has been previously assumed. This result carries implications for the interpretation of isotope signals recorded in geologic sulfate archives.

Declaration of Competing Interest

The authors declare that they have no known competing financial interests or personal relationships that could have appeared to influence the work reported in this paper.

Acknowledgements

The computations in this paper were run on the FASRC Cannon cluster supported by the FAS Division of Science Research Computing Group at Harvard University. This result is part of a project that has received funding from the European Research Council (ERC) under the European Union's Horizon 2020 research and innovation program (Grant agreement No. 946150, to J.D.H.). Additional funding was provided by the American Chemical Society Petroleum

Research Fund (Grant No. 59455-ND2, to J.D.H. and D.T.J.). We thank Nir Galili, Itay Halevy, and Cornelia Mertens for helpful discussions. We thank Associate Editor Marc Blanchard, Daniel Eldridge, and one anonymous reviewer for their comments and critiques that greatly improved and strengthened this work.

Appendix A. Supplementary material

Supplementary material associated with this article can be found, in the online version, at <https://doi.org/10.1016/j.gca.2022.07.011>.

References

- Balci, N., Shanks III, W.C., Mayer, B., Mandernack, K.W., 2007. Oxygen and sulfur isotope systematics of sulfate produced by bacterial and abiotic oxidation of pyrite. *Geochim. Cosmochim. Acta* 71, 3796–3811.
- Bao, H., Lyons, J., Zhou, C., 2008. Triple oxygen isotope evidence for elevated CO₂ levels after a Neoproterozoic glaciation. *Nature* 453, 504–506.
- Barkan, E., Luz, B., 2005. High precision measurements of ¹⁷O/¹⁶O and ¹⁸O/¹⁶O ratios in H₂O. *Rapid Comm. Mass Spec.* 19, 3737–3742.
- Becke, A.D., 1993. A new mixing of Hartree-Fock and local density-functional theories. *J. Chem. Phys.* 98, 1372–1377.
- Benkovic, S., Hevey, R., 1970. Studies in sulfate esters. V. The mechanism of hydrolysis of phenyl phosphosulfate, a model system for 3'-phosphoadenosine 5'-phosphosulfate. *J. Am. Chem. Soc.* 92, 4971–4977.
- Benson, B.B., Krause Jr., D., 1984. The concentration and isotopic fractionation of oxygen dissolved in freshwater and seawater in equilibrium with the atmosphere. *Limnol. Oceanogr.* 29, 620–632.
- Berner, R.A., 1984. Sedimentary pyrite formation: an update. *Geochim. Cosmochim. Acta* 48, 605–615.
- Berner, R.A., 2001. Modeling atmospheric O₂ over Phanerozoic time. *Geochim. Cosmochim. Acta* 65, 685–694.
- Bertran, E., Waldeck, A., Wing, B.A., Halevy, I., Leavitt, W.D., Bradley, A.S., Johnston, D.T., 2020. Oxygen isotope effects during microbial sulfate reduction: applications to sediment cell abundances. *ISME J.* 14, 1508–1519.
- Betts, R., Voss, R., 1970. The kinetics of oxygen exchange between the sulfite ion and water. *Can. J. Chem.* 48, 2035–2041.
- Bigeleisen, J., Goepfert, Mayer M., 1947. Calculation of equilibrium constants for isotopic exchange reactions. *J. Chem. Phys.* 15, 261–267.
- Blättler, C.L., Claire, M., Prave, A., Kirsimäe, K., Higgins, J.A., Medvedev, P., Romashkin, A., Rychanchik, D., Zerkle, A., Paiste, K., Kreitsmann, T., Miller, I., Hayles, J., Bao, H., Turchyn, A., Warke, M., Lepland, A., 2018. Two-billion-year-old evaporites capture Earth's great oxidation. *Science* 360, 320–323.
- Born, M., Huang, K., 1954. *Dynamical Theory of Crystal Lattices*. Clarendon Press, Oxford, UK.
- Born, M., Oppenheimer, J.R., 1927. Zur quantentheorie der molekeln. *Ann. Phys.* 389, 457–484.
- Brandt, C., van Eldik, R., 1995. Transition metal-catalyzed oxidation of sulfur(IV) oxides. Atmospheric-relevant processes and mechanisms. *Chem. Rev.* 95, 119–190.
- Brunner, B., Einsiedl, F., Arnold, G.L., Müller, I., Templer, S., Bernasconi, S.M., 2012. The reversibility of dissimilatory sulphate reduction and the cell-internal multi-step reduction of sulphate to sulphate: insights from the oxygen isotope composition of sulphate. *Isotopes Environ. Health Stud.* 48, 33–54.
- Burke, A., Present, T.M., Paris, G., Rae, E.C., Sandilands, B.H., Gaillardet, J., Peucker-Ehrenbrink, B., Fischer, W.W., McClelland, J.W., Spencer, R.G., Voss, B.M., Adkins, J.F., 2018. Sulfur isotopes in rivers: insights into global weathering budgets, pyrite oxidation, and the modern sulfur cycle. *Earth Planet. Sci. Lett.* 496, 168–177.
- Burt, E.I., Bill, M., Conrad, M.E., Quispe, A.J.C., Christensen, J.N., Hilton, R.G., Dellinger, M., West, A.J., 2021. Conservative transport of dissolved sulfate across the Rio Madre de Dios floodplain in Peru. *Geology* 49, 1064–1068.
- Cao, X., Bao, H., 2021. Small triple oxygen isotope variations in sulfate: mechanisms and applications. *Rev. Mineral. Geochem.* 86, 463–488.
- Cao, X., Liu, Y., 2011. Equilibrium mass-dependent fractionation relationships for triple oxygen isotopes. *Geochim. Cosmochim. Acta* 75, 7435–7445.
- Cao, X., Liu, Y., 2012. Theoretical estimation of the equilibrium distribution of clumped isotopes in nature. *Geochim. Cosmochim. Acta* 77, 292–303.
- Chang, S.J., Blake, R.E., 2015. Precise calibration of equilibrium oxygen isotope fractionations between dissolved phosphate and water from 3 to 37 °C. *Geochim. Cosmochim. Acta* 150, 314–329.
- Chiba, H., Sakai, H., 1985. Oxygen isotope exchange rate between dissolved sulfate and water at hydrothermal temperatures. *Geochim. Cosmochim. Acta* 49, 993–1000.
- Chiba, H., Kusakabe, M., Hirano, S.I., Matsuo, S., Shigeyuki, S., 1981. Oxygen isotope fractionation factors between anhydrite and water from 100 to 550 °C. *Earth Planet. Sci. Lett.* 53, 55–62.
- Chiba, H., Uchiyama, N., Teagle, D.A., 1998. Stable isotope study of anhydrite and sulfide minerals at the TAG hydrothermal mound, Mid-Atlantic Ridge, 26° N. In: Herzig, P., Miller, S., Zierenberg, R. (Eds.), *Proceedings of the Ocean Drilling Program, Scientific Results*. Texas A&M University, Texas, USA, vol. 158, pp. 85–90.
- Clements, T.G., Deyerl, J.J., Continetti, R.E., 2002. Dissociative photodetachment dynamics of S₂O₇²⁻. *J. Phys. Chem. A* 106, 279–284.
- Coplen, T.B., Kendall, C., 2000. Stable hydrogen and oxygen isotope ratios for selected sites of the US Geological Survey's NASQAN and benchmark surface-water networks. Tech. Rep., United States Geological Survey, Reston, VA, USA.
- Crockford, P.W., Hayles, J.A., Bao, H., Planavsky, N.J., Bekker, A., Fralick, P.W., Halverson, G.P., Hui, T.H., Peng, Y., Wing, B.A., 2018. Triple oxygen isotope evidence for limited mid-Proterozoic primary productivity. *Nature* 559, 613–616.
- Crockford, P.W., Kunzmann, M., Bekker, A., Hayles, J., Bao, H., Halverson, G.P., Peng, Y., Bui, T.H., Cox, G.M., Gibson, T.M., Wörndle, S., Rainbird, R., Lepland, A., Swanson-Hysell, N.L., Master, S., Sreenivas, B., Kuznetsov, A., Krupnik, V., Wing, B.A., 2019. Claypool continued: extending the isotopic record of sedimentary sulfate. *Chem. Geol.* 513, 200–225.
- Damian, Risberg E., Eriksson, L., Mink, J., Pattersson, L.G., Skripkin, M.Y., Sandström, M., 2007. Sulfur X-ray absorption and vibration spectroscopic study of sulfur dioxide, sulfite, and sulfonate solutions and of the substituted sulfonate ions X₃CSO₃⁻ (X = H, Cl, F). *Inorg. Chem.* 46, 8332–8348.
- Eldridge, D.L., Guo, W., Farquhar, J., 2016. Theoretical estimates of equilibrium sulfur isotope effects in aqueous sulfur systems: highlighting the role of isomers in the sulfite and sulfoxylate systems. *Geochim. Cosmochim. Acta* 195, 171–200.
- Eldridge, D.L., Mysen, B.O., Cody, G.D., 2018. Experimental estimation of the bisulfite isomer quotient as a function of temperature: implications for sulfur isotope fractionations in aqueous sulfite solutions. *Geochim. Cosmochim. Acta* 220, 309–328.
- Eldridge, D.L., Kamyshny Jr., A., Farquhar, J., 2021. Theoretical estimates of equilibrium sulfur isotope effects among aqueous polysulfur and associated compounds with applications to authigenic pyrite formation and hydrothermal disproportionation reactions. *Geochim. Cosmochim. Acta* 310, 281–319.
- Fike, D.A., Bradley, A.S., Rose, C.V., 2015. Rethinking the ancient sulfur cycle. *Ann. Rev. Earth Planet. Sci.* 43, 593–622.
- Finster, K., Liesack, W., Thamdrup, B., 1998. Elemental sulfur and thiosulfate disproportionation by *Desulfocapsa sulfoexigens* sp. nov., a new anaerobic bacterium isolated from marine surface sediment. *Appl. Environ. Microbiol.* 64, 119–125.
- Frisch, M.J., Head-Gordon, M., Pople, J.A., 1990. A direct MP2 gradient method. *Chem. Phys. Lett.* 166, 275–280.
- Frisch, M.J., Trucks, G.W., Schlegel, H.B., Scuseria, G.E., Robb, M.A., Cheeseman, J.R., Scalmani, G., Barone, V., Petersson, G.A., Nakatsuji, H., Li, X., Caricato, M., Marenich, A.V., Bloino, J., Janesko, B.G., Gomperts, R., Mennucci, B., Hratchian, H. P., Ortiz, J.V., Izmaylov, A.F., Sonnenberg, J.L., Williams-Young, D., Ding, F., Lipparini, F., Egidi, F., Goings, J., Peng, B., Petrone, A., Henderson, T., Ranasinghe, D., Zakrzewski, V.G., Gao, J., Rega, N., Zheng, G., Liang, W., Hada, M., Ehara, M., Toyota, K., Fukuda, R., Hasegawa, J., Ishida, M., Nakajima, T., Honda, Y., Kitao, O., Nakai, H., Vreven, T., Throssell, K., Montgomery, Jr. J.A., Peralta, J.E., Ogliaro, F., Bearpark, M.J., Heyd, J.J., Brothers, E.N., Kudin, K.N., Staroverov, V.N., Keith, T.A., Kobayashi, R., Normand, J., Raghavachari, K., Rendell, A.P., Burant, J.C., Iyengar, S. S., Tomasi, J., Cossi, M., Millam, J.M., Klene, M., Adamo, C., Cammi, R., Ochterski, J.W., Martin, R.L., Morokuma, K., Farkas, O., Foresman, J.B., Fox, D.J., 2016. *Gaussian 16 Revision C.01*. Tech. Rep., Gaussian Inc., Wallingford, CT, USA.
- Goldberg, R., Parker, V., 1985. Thermodynamics of solution of SO₂(g) in water and of aqueous sulfur dioxide solutions. *J. Res. Nat. Bureau Stand.* 90, 341–358.
- Guo, W., Zhou, C., 2019. Triple oxygen isotope fractionation in the DIC-H₂O-CO₂ system: a numerical framework and its implications. *Geochim. Cosmochim. Acta* 246, 541–564.
- Hayles, J., Gao, C., Cao, X., Liu, Y., Bao, H., 2018. Theoretical calibration of the triple oxygen isotope thermometer. *Geochim. Cosmochim. Acta* 235, 237–245.
- Hemingway, J.D., Olson, H., Turchyn, A.V., Tipper, E.T., Bickle, M.J., Johnston, D.T., 2020. Triple oxygen isotope insight into terrestrial pyrite oxidation. *Proc. Natl. Acad. Sci.* 117, 7650–7657.
- Hill, P.S., Tripathi, A.K., Schauble, E.A., 2014. Theoretical constraints on the effects of pH, salinity, and temperature on clumped isotope signatures of dissolved inorganic carbon species and precipitating carbonate minerals. *Geochim. Cosmochim. Acta* 125, 610–652.
- Hochlaf, M., Linguerr, R., Cheraki, M., Ayari, T., Ben, Said R., Feifel, R., Chambaud, G., 2021. S₂O₇²⁻ (q = 0, 1, and 2) molecular systems: Characterization and atmospheric planetary implications. *J. Phys. Chem. A* 125, 1958–1971.
- Horita, J., Cole, D.R., Wesolowski, D.J., 1995. The activity-composition relationship of oxygen and hydrogen isotopes in aqueous salt solutions: III. Vapor-liquid water equilibrium of NaCl solutions to 350 °C. *Geochim. Cosmochim. Acta* 59, 1139–1151.
- Horita, J., Rozanski, K., Cohen, S., 2008. Isotope effects in the evaporation of water: a status report of the Craig-Gordon model. *Isotopes Environ. Health Stud.* 44, 23–49.
- Horner, D.A., Connick, R.E., 1986. Equilibrium quotient for the isomerization of bisulfite ion from HSO₃⁻ to SO₃H⁻. *Inorg. Chem.* 25, 2414–2417.
- Irikura, K.K., 2007. Experimental vibrational zero-point energies: diatomic molecules. *J. Phys. Chem. Ref. Data* 36, 389–397.
- Irikura, K.K., Johnson III, R.D., Kacker, R.N., 2005. Uncertainties in scaling factors for ab initio vibrational frequencies. *J. Phys. Chem. A* 109, 8430–8437.
- Irikura, K.K., Johnson, R.D., Kacker, R., Kessel, R., 2009. Uncertainties in scaling factors for ab initio vibrational zero-point energies. *J. Chem. Phys.* 130, 114102.

- Johnson III R.D., (Ed.), 2020. NIST Computational Chemistry Comparison and Benchmark Database. No. 101 in 21. National Institute of Standards and Technology, <http://cccbdb.nist.gov/>.
- Johnston, F., McAmish, L., 1973. A study of the rates of sulfur production in acid thiosulfate solutions using S-35. *J. Colloid Interface Sci.* 42, 112–119.
- Jørgensen, B.B., 1990. A thiosulfate shunt in the sulfur cycle of marine sediments. *Science* 249, 152–154.
- Kemeny, P., Lopez, G., Dalleska, N., Torres, M., Burke, A., Bhatt, M., West, A.J., Hartmann, J., Adkins, J.F., 2021. Sulfate sulfur isotopes and major ion chemistry reveal that pyrite oxidation counteracts CO₂ drawdown from silicate weathering in the Langtang-Trisuli-Narayani River system, Nepal Himalaya. *Geochim. Cosmochim. Acta* 294, 43–69.
- Kendall, R.A., Dunning Jr., T.H., Harrison, R.J., 1992. Electron affinities of the first-row atoms revisited. Systematic basis sets and wave functions. *J. Chem. Phys.* 96, 6796–6806.
- Killingsworth, B.A., Bao, H., Kohl, I.E., 2018. Assessing pyrite-derived sulfate in the Mississippi River with four years of sulfur and triple-oxygen isotope data. *Environ. Sci. Technol.* 52, 6126–6136.
- Kohl, I., Bao, H., 2011. Triple-oxygen-isotope determination of molecular oxygen incorporation in sulfate produced during abiotic pyrite oxidation (pH = 2–11). *Geochim. Cosmochim. Acta* 75, 1785–1798.
- Kohl, I., Asatryan, R., Bao, H., 2012. No oxygen isotope exchange between water and APS-sulfate at surface temperature: evidence from quantum chemical modeling and triple-oxygen isotope experiments. *Geochim. Cosmochim. Acta* 95, 106–118.
- Kusakabe, M., Robinson, B.W., 1977. Oxygen and sulfur isotope equilibria in the BaSO₄ – HSO₄⁻ – H₂O system from 100 to 350 °C and applications. *Geochim. Cosmochim. Acta* 41, 1033–1040.
- Lee, C., Yang, W., Parr, R.G., 1988. Development of the Colle-Salvetti correlation-energy formula into a functional of the electron density. *Phys. Rev. B* 37, 785–789.
- Li, X., Liu, Y., 2011. Equilibrium Se isotope fractionation parameters: a first-principles study. *Earth Planet. Sci. Lett.* 304, 113–120.
- Li, X., Zhao, H., Tang, M., Liu, Y., 2009. Theoretical prediction for several important equilibrium Ge isotope fractionation factors and geological implications. *Earth Planet. Sci. Lett.* 287, 1–11.
- Littlejohn, D., Walton, S., Chang, S.G., 1992. A Raman study of the isomers and dimer of hydrogen sulfite ion. *Appl. Spec.* 46, 848–851.
- Liu, Q., Liu, Y., 2016. Clumped-isotope signatures at equilibrium of CH₄, NH₃, H₂O, H₂S and SO₂. *Geochim. Cosmochim. Acta* 175, 252–270.
- Liu, Q., Tossell, J.A., Liu, Y., 2010. On the proper use of the Bigeleisen-Mayer equation and corrections to it in the calculation of isotopic fractionation equilibrium constants. *Geochim. Cosmochim. Acta* 74, 6965–6983.
- Lloyd, R., 1968. Oxygen isotope behavior in the sulfate-water system. *J. Geophys. Res.* 73, 6099–6110.
- Luz, B., Barkan, E., 2009. Net and gross oxygen production from O₂/Ar, ¹⁷O/¹⁶O, and ¹⁸O/¹⁶O ratios. *Aquat. Microb. Ecol.* 56, 133–145.
- Marsden, C.J., Smith, B.J., 1990. An ab initio study of many isomers of S₂O₂. A combined theoretical and experimental analysis of the harmonic force field and molecular structure of cis-planar OSSO. *Chem. Phys.* 141, 335–353.
- Masterson, A., Alperin, M.J., Berelson, W.M., Johnston, D.T., 2018. Interpreting multiple sulfur isotope signals in modern anoxic sediments using a full diagenetic model (California-Mexico Margin: Alfonso Basin). *Am. J. Sci.* 318, 459–490.
- Masterson, A.J., Alperin, M.J., Arnold, G.L., Berelson, W.M., Jørgensen, B.B., Røy, H., Johnston, D.T., 2022. Understanding the isotopic composition of sedimentary sulfide: a multiple sulfur isotope diagenetic model for Aarhus Bay. *Am. J. Sci.* 322, 1–27.
- Matsuhisa, Y., Goldsmith, J.R., Clayton, R.N., 1978. Mechanisms of hydrothermal crystallization of quartz at 250 °C and 15 kbar. *Geochim. Cosmochim. Acta* 42, 173–182.
- Merrick, J.P., Moran, D., Radom, L., 2007. An evaluation of harmonic vibrational frequency scale factors. *J. Phys. Chem. A* 111, 11683–11700.
- Millero, F.J., Hershey, J.P., Johnson, G., Zhang, J.Z., 1989. The solubility of SO₂ and the dissociation of H₂SO₃ in NaCl solutions. *J. Atmos. Chem.* 8, 377–389.
- Mizutani, Y., Rafter, T.A., 1969. Oxygen isotopic composition of sulphates—part 3. Oxygen isotopic fractionation in the bisulphate ion–water system. *N.Z.J. Sci.* 12, 54–59.
- Møller, C., Plesset, M., 1934. Note on an approximation treatment for many-electron systems. *Phys. Rev.* 46, 618–622.
- Müller, I.A., Brunner, B., Breuer, C., Coleman, M., Bach, W., 2013a. The oxygen isotope equilibrium fractionation between sulfite species and water. *Geochim. Cosmochim. Acta* 120, 562–581.
- Müller, I.A., Brunner, B., Coleman, M., 2013b. Isotopic evidence of the pivotal role of sulfite oxidation in shaping the oxygen isotope signature of sulfate. *Chem. Geol.* 354, 186–202.
- Neubauer, C., Crémère, A., Wang, X.T., Nivedita, T., Sessions, A.L., Adkins, J.F., Dalleska, N.F., Turchyn, A.V., Clegg, J.A., Moradian, A., Sweredoski, M.J., Garbis, S. D., Eiler, J.M., 2020. Stable isotope analysis of intact oxyanions using electrospray quadrupole-orbitrap mass spectrometry. *Anal. Chem.* 92, 3077–3085.
- Novoa, J.J., Sosa, C., 1995. Evaluation of the density function approximation on the computation of hydrogen bond interactions. *J. Phys. Chem.* 99, 15837–15845.
- O’Neil, J.R., Clayton, R.N., Mayeda, T.K., 1969. Oxygen isotope fractionation in divalent metal carbonates. *J. Chem. Phys.* 51, 5547–5558.
- Pryor, W.A., Tonellato, U., 1967. Nucleophilic displacement at sulfur III. The exchange of oxygen-18 between sodium thiosulfate-¹⁸O and water. *J. Am. Chem. Soc.* 89, 3379–3386.
- Pye, C.C., Rudolph, W.W., 2001. An ab initio and Raman investigation of sulfate ion hydration. *J. Phys. Chem. A* 105, 905–912.
- Ramírez-Solis, A., Jolibois, F., Maron, L., 2011. Born-Oppenheimer DFT molecular dynamics studies of S₂O₂: Non-harmonic effects on the lowest energy isomers. *Chem. Phys. Lett.* 510, 21–26.
- Redlich, O., 1935. Eine allgemeine beziehung zwischen den schwingungsfrequenzen isotope molekl. *Z. Phys. Chem.* 28, 371–382.
- Richet, P., Bottinga, Y., Javoy, M., 1977. A review of hydrogen, carbon, nitrogen, oxygen, sulphur, and chlorine stable isotope fractionation among gaseous molecules. *Ann. Rev. Earth Planet. Sci.* 5, 65–110.
- Rimstidt, J.D., Vaughan, D.J., 2003. Pyrite oxidation: a state-of-the-art assessment of the reaction mechanism. *Geochim. Cosmochim. Acta* 67, 873–880.
- Schauble, E.A., Young, E.D., 2021. Mass dependence of equilibrium oxygen isotope fractionation in carbonate, nitrate, oxide, perchlorate, phosphate, silicate, and sulfate minerals. *Rev. Mineral. Geochem.* 86, 137–178.
- Schoonen, M.A., Harrington, A.D., Laffers, R., Strongin, D.R., 2010. Role of hydrogen peroxide and hydroxyl radical in pyrite oxidation by molecular oxygen. *Geochim. Cosmochim. Acta* 74, 4971–1987.
- Scott, A.P., Radom, L., 1996. Harmonic vibrational frequencies: an evaluation of Hartree-Fock, Møller-Plesset, quadratic configuration interaction, density functional theory, and semiempirical scale factors. *J. Phys. Chem.* 100, 16502–16513.
- Scuseria, G.E., Janssen, C.L., Schaefer, H.F., 1988. An efficient reformulation of the closed-shell coupled cluster single and double excitation (CCSD) equations. *J. Chem. Phys.* 89, 7382–7387.
- Sharp, Z.D., Wostbrock, J.A., 2021. Standardizations for the triple oxygen isotope system: waters, silicates, carbonates, air, and sulfates. *Rev. Mineral. Geochem.* 86, 179–196.
- Sutherland, K.M., Hemingway, J.D., Johnston, D.T., 2022. The influence of reactive oxygen species on “respiration” isotope effects. *Geochim. Cosmochim. Acta* 324, 86–101.
- Teagle, D.A., Alt, J.C., Halliday, A.N., 1998. Tracing the chemical evolution of fluids during hydrothermal recharge: constraints from anhydrite recovered in ODP Hole 504B. *Earth Planet. Sci. Lett.* 155, 167–182.
- Thiemens, M.H., Lin, M., 2021. Discoveries of mass independent isotope effects in the solar system: past, present, and future. *Rev. Mineral. Geochem.* 86, 35–95.
- Turchyn, A.V., Tipper, E.T., Galy, A., Lo, J.K., Bickle, M.J., 2013. Isotope evidence for secondary sulfide precipitation along the Marsiyandi River, Nepal, Himalayas. *Earth Planet. Sci. Lett.* 374, 36–46.
- Urey, H.C., 1947. The thermodynamic properties of isotopic substances. *J. Chem. Soc.* 562–581.
- Vairavamurthy, A., Manowitz, B., Luther III, G., Jeon, Y., 1993. Oxidation state of sulfur in thiosulfate and implications for anaerobic energy metabolism. *Geochim. Cosmochim. Acta* 57, 1619–1623.
- Waldeck, A., Cowie, B., Bertran, E., Wing, B., Halevy, I., Johnston, D., 2019. Deciphering the atmospheric signal in marine sulfate oxygen isotope composition. *Earth Planet. Sci. Lett.* 522, 12–19.
- Wankel, S.D., Bradley, A.S., Eldridge, D.L., Johnston, D.T., 2014. Determination and application of the equilibrium oxygen isotope effect between water and sulfite. *Geochim. Cosmochim. Acta* 125, 694–711.
- Weinzierl, C., Regelous, M., Haase, K., Bach, W., Böhm, F., Garbe-Schönberg, D., Sun, Y., Joachimski, M., Krumm, S., 2018. Cretaceous seawater and hydrothermal fluid compositions recorded in abiogenic carbonates from the Troodos Ophiolite, Cyprus. *Chem. Geol.* 494, 43–55.
- Williamson, M.A., Rimstidt, J.D., 1994. The kinetics and electrochemical rate-determining step of aqueous pyrite oxidation. *Geochim. Cosmochim. Acta* 58, 5443–5454.
- Wilson, E.B., Decius, J.G., Cross, P.G., 1955. *Molecular Vibrations*. McGraw-Hill, New York, NY, USA.
- Wing, B.A., Halevy, I., 2014. Intracellular metabolite levels shape sulfur isotope fractionation during microbial sulfate reduction. *Proc. Natl. Acad. Sci.* 111, 18116–18125.
- Xu, Y., Schoonen, M.A., 1995. The stability of thiosulfate in the presence of pyrite in low-temperature aqueous solutions. *Geochim. Cosmochim. Acta* 59, 4605–4622.
- Xu, Y., Schoonen, M., Nordstrom, D., Cunningham, K., Ball, J., 1998. Sulfur geochemistry of hydrothermal waters in Yellowstone National Park: I. The origin of thiosulfate in hot spring waters. *Geochim. Cosmochim. Acta* 62, 3729–3743.
- Yeung, L.Y., Hayles, J.A., 2021. Climbing to the top of Mount Fuji: uniting theory and observations of oxygen triple isotope systematics. *Rev. Mineral. Geochem.* 86, 97–137.
- Young, E.D., Galy, A., Nagahara, H., 2002. Kinetic and equilibrium mass-dependent isotope fractionation laws in nature and their geochemical and cosmochemical significance. *Geochim. Cosmochim. Acta* 66, 1095–1104.
- Zeebe, R.E., 2010. A new value for the stable oxygen isotope fractionation between dissolved sulfate ion and water. *Geochim. Cosmochim. Acta* 74, 818–828.
- Zhang, Y., Liu, Y., 2018. The theory of equilibrium isotope fractionations for gaseous molecules under super-cold conditions. *Geochim. Cosmochim. Acta* 238, 123–149.